A THREE DIMENSIONAL FINITE ELEMENT METHOD AND MULTIGRID SOLVER FOR A DARCY-STOKES SYSTEM AND APPLICATIONS TO VUGGY POROUS MEDIA

by

MARIO SAN MARTIN GOMEZ, M.S.

DISSERTATION

Presented to the Faculty of the Graduate School of
The University of Texas at Austin
in Partial Fulfillment
of the Requirements
for the Degree of

DOCTOR OF PHILOSOPHY

THE UNIVERSITY OF TEXAS AT AUSTIN
May 2007

The Dissertation Committee for Mario San Martin Gomez
Certifies that this is the approved version of the following dissertation:

A THREE DIMENSIONAL FINITE ELEMENT METHOD AND MULTIGRID SOLVER FOR A DARCY-STOKES SYSTEM AND APPLICATIONS TO VUGGY POROUS MEDIA

Committee:

Todd J. Arbogast, Supervisor

Steven L. Bryant

Irene Gamba

Oscar Gonzales

Jack Xin

Acknowledgements

First and foremost, I thank my supervisor, Professor Todd Arbogast, for his encouragement and for suggesting a thesis problem that turned out to be both interesting and challenging. I also acknowledge Professors Irene Gamba and Oscar Gonzalez for being excellent teachers and inspiring scientists. Our graduate coordinator, Mrs. Nancy Lamm, was always extremely helpful and I am grateful to her. I also thank my colleagues Rohit Ghosh and Magdalena Czubak for their sincere friendship.

A THREE DIMENSIONAL FINITE ELEMENT METHOD AND MULTIGRID SOLVER FOR A DARCY-STOKES SYSTEM AND APPLICATIONS TO VUGGY POROUS MEDIA

Publication No. ____________________

Mario San Martin Gomez, Ph.D.
The University of Texas at Austin, 2007

Supervisor: Todd J. Arbogast

A vuggy porous medium is one with many small cavities called *vugs,* which are interconnected in complex ways forming channels that can support high flow rates. Flow in such a medium can be modeled by combining Darcy flow in the rock matrix with Stokes flow in the vugs. We develop a finite element for the numerical solution of this problem in three dimensions, which converges at the optimal rate.

We design a multigrid method to solve a saddle point linear system that comes from this discretization. The intertwining of the Darcy and Stokes subdomains in a natural vuggy medium makes the resulting matrix highly oscillating, or ill-conditioned. The velocity field we are trying to compute is also very irregular and its tangential component might be discontinuous at the Darcy-Stokes interface. This imposes a difficulty in defining intergrid transfer operators. Our definition is based on mass conservation and the analysis of the orders of magnitude of the solution. A new smoother is developed that works well for this ill-conditioned problem. We prove that coarse grid equations at all levels are well posed saddle point systems. Our algorithm has a measured convergence factor independent of the size of the system.

We then use our solver to study transport and flow properties of vuggy media by simulations. We analyze the results of our transport simulations and compare them to experimental results. We study the influence of vug geometry on the macroscopic flow properties of a three dimensional vuggy porous medium.

Table of Contents

List of Figures

Chapter 1

Introduction

This work is related to the computational modeling of fluid flow in subsurface systems that consist of a vuggy porous medium. Vugs are small cavities that have a much larger size than the intergranular pore space. They are spread throughout the rock and have a major effect on the flow and transport properties of such a medium. This fact has been confirmed by field and laboratory experiments. In this dissertation, we improve our understanding of this effect through numerical simulations.

The study of this type of system has both, theoretical and practical importance. Many of the world's oil reservoirs and water aquifers contain vuggy rocks. Therefore, a better understanding of their flow and transport properties, and the development of simulation methods that allow us to make predictions, is of economic and environmental interest. For example, it could increase our knowledge about the movement of contaminants in the subsurface and help in the prevention and remediation of water contamination.

Some of the difficulties encountered in the mathematical modeling of flow in a vuggy medium come from the heterogeneity of the system. In the cavities or vugs, low Reynolds number flow is expected and it can be described by Stokes equation [4]. Flow in the porous matrix obeys Darcy's law [8, 21, 29, 31]. When these equations are combined with mass conservation, the resulting elliptic system can be written in mixed formulation. The interaction at the interface between the porous matrix and the vugs is described by the Beavers-Joseph-Saffman boundary condition [9, 26], which allows for a discontinuity of the tangential component of the velocity at the interface.

Numerical techniques have been developed for the treatment of Darcy-Stokes systems, but most of them are appropriate for the case when the open cavity and the porous medium are well separated [27, 20, 17]. A step forward was taken in [4], where a finite element method is proposed that uses Stokes elements suitably modified near the interface to account for the tangential discontinuity. Besides capturing the different regularities of the solution in the Darcy and Stokes subdomains, the main advantage of this method is that it works for the case when these two subdomains are totally intertwined, as occurs in a vuggy medium. These finite elements were defined for two dimensional domains; we extend them to three dimensions in this dissertation.

Once the differential system has been discretized, the next problem is to solve the corresponding algebraic linear system. Because the flow is described by different equations in the vugs and in the porous matrix, and both subdomains are intertwined, the resulting matrix is highly oscillating and hence, ill-conditioned. In [4], the authors use an Uzawa iterative procedure to solve the system. Such an ill-conditioned system requires an effective preconditioner in order for an iterative method to converge at a reasonable rate. They utilized the block structure of the matrix to approximate its inverse, and designed a preconditioner which turned out to be effective, but expensive to compute and not suitable to be adapted to a parallel code. On the other hand, using a simpler preconditioner reduces the Uzawa algorithm rate of convergence considerably, since the slow components of the error are difficult to eliminate. This was our motivation for developing a multigrid method for the solution of the system. The design of the multigrid algorithm is a central topic of this work. The difficulty comes from the fact that the solution of this oscillating system is very irregular and may have big jumps of several orders of magnitude from one grid point to the next one. Hence, the conventional methods that are used to define intergrid transfer operators are not suitable here. Our definition of prolongation and restriction operators is based on an interpretation of coarse grid quantities as fluxes, the use of mass conservation and the analysis of the order of magnitude of the solution in the Stokes and Darcy subdomains. We prove that the coarse grid equations at all levels are well posed and show that our algorithm has a measured convergence factor independent of the size of the system. Our method is also suitable for parallelization, which we plan to do in the future.

We then use our solver to investigate by simulations the transport and flow properties of vuggy porous media. Flow properties had been previously studied in the two dimensional case in [5] and [15]. We confirm and extend these computational results in three dimensions. Transport properties were studied experimentally in [32]. A pulse of tracer was injected into a sample of carbonate rock and the effluent tracer concentration was measured at different times. A plot with a characteristic shape was consistently obtained and one of its most interesting features was the presence of plateaus during the fast initial increase and right after the abrupt drop in the concentration history. It is proposed in [32] that the plateaus are mainly due to the presence of dead-end vugs. We simulated simple cases of vug geometry and our computational results are consistent with an alternative mechanism.

The outline of the thesis is as follows. In Chapter 2 we recall the mathematical formulation of a flow in a vuggy porous medium and the discretization of the resulting differential system by the finite element method introduced in [4]. The new aspect is the more general treatment of the boundary conditions, which has theoretical and practical implications. We also explain the generalization of the finite element method of [4] to the three dimensional case. In Chapter 3 we develop our multigrid algorithm for the solution of the discretized system and prove that the coarse-grid equations are well posed at all levels. In Chapter 4 we illustrate the performance of our multigrid method and show that its measured convergence factor is independent of the size of the system. In Chapter 5 we discuss the tracer experiments of [32] and present a series of transport simulations in vuggy media with characteristic vug geometries. Based on our simulation results, we propose a mechanism that explains some of the experimental observations. In Chapter 6 we investigate computationally the effect of vug shape and connectedness on the flow properties of vuggy media in three dimensions, using a macro-model obtained in [6] from homogenization theory. We summarize our work and conclusions, and comment on future work, in Chapter 7.

Chapter 2

The Mathematical Model and its Discretization

In this chapter, we first present the Darcy-Stokes equations governing flow in a vuggy porous medium at a small scale (but above the pore scale). We then discuss its finite element approximation, defining along the way a new finite element suitable for three dimensional problems.

2.1 Mathematical formulation of flow in a vuggy porous medium

The model we will refer to was introduced in [4]. We recall it here both for completeness and to explain in more detail the different types of boundary conditions, which is relevant to the proof of Theorem 3.4.3 below. The model describes the flow of an incompressible fluid in a porous medium with many small cavities which are relatively large compared to the dimensions of the pores, distributed throughout the whole domain. The domain is a subset of $\mathbb{R}^3$, denoted by Ω. The flow in the subdomain Ω_s, corresponding to the cavities, is described by the Stokes equation. The flow in the subdomain Ω_d, corresponding to the porous matrix, is described by Darcy's law. Thus, Ω is the union of Ω_d, Ω_s and the interface between them, which will be denoted by

Γ. On Γ we have the so-called Beavers-Joseph-Saffman boundary condition [9, 26], which allows for a discontinuity of the tangential component of the velocity across the interface.

Throughout this chapter, $\mathbf{u}_s$ and $\mathbf{u}_d$ denote the velocity of the fluid in the subdomains Ω_s and Ω_d respectively. Similarly, p_s and p_d denote the pressure in the respective subdomains. We let $D\mathbf{u}$ denote the symmetric gradient of $\mathbf{u}$, i.e., $(D\mathbf{u})_{i,j} = \frac{1}{2}(\partial_j u_i + \partial_i u_j)$, $i, j = 1, 2, 3$. Also, $\mu > 0$ is the fluid viscosity, K the rock permeability, $\alpha > 0$ the Beavers-Joseph coefficient, f represents a force term such as gravity, and g an external source or sink. Let ν denote the outer unit normal to $\partial\Omega$ and, on the interface Γ, the outer unit normal to $\partial\Omega_s$, and let τ_1 and τ_2 denote the unit tangent to Γ or to $\partial\Omega$. Let C be a subset of $\partial\Omega$, and u_N and p_B square-integrable functions defined on C and $\partial\Omega \setminus C$, respectively. The governing equations follow (see references [4, 9, 26, 19]).

Vuggy region (Stokes equations)

$$-2\mu\nabla \cdot D\mathbf{u}_s + \nabla p_s = f \quad \text{in } \Omega_s, \tag{2.1}$$

$$\nabla \cdot \mathbf{u}_s = g \quad \text{in } \Omega_s, \tag{2.2}$$

Rock matrix (Darcy equations)

$$\mu K^{-1}\mathbf{u}_d + \nabla p_d = f \quad \text{in } \Omega_d, \tag{2.3}$$

$$\nabla \cdot \mathbf{u}_d = g \quad \text{in } \Omega_d, \tag{2.4}$$

Interface

$$\mathbf{u}_s \cdot \nu = \mathbf{u}_d \cdot \nu \qquad \text{on } \Gamma, \tag{2.5}$$

$$2\nu \cdot D\mathbf{u}_s \cdot \tau_i = -\alpha K^{-1/2} \mathbf{u}_s \cdot \tau_i \quad \text{on } \Gamma,\ i = 1, 2, \tag{2.6}$$

$$2\mu\nu \cdot D\mathbf{u}_s \cdot \nu = p_s - p_d \qquad \text{on } \Gamma, \tag{2.7}$$

Outer boundary

$$\mathbf{u} \cdot \nu = u_N \quad \text{on } C, \tag{2.8}$$

$$p - 2\mu\nu \cdot D\mathbf{u} \cdot \nu = p_B \quad \text{on } \partial\Omega \setminus C, \tag{2.9}$$

$$\mathbf{u} \cdot \tau_i = 0 \qquad \text{on } \partial\Omega \cap \partial\Omega_s,\ i = 1, 2 \tag{2.10}$$

We now derive a variational formulation of (2.1)–(2.10) in a suitable function space. We search for velocity $\mathbf{u}$ and pressure p such that $(\mathbf{u}, p) \in (\bar{\mathbf{V}}, W)$, where $\bar{\mathbf{V}}$ is the affine space

$$\begin{aligned} \bar{\mathbf{V}} = \bar{\mathbf{V}}_{u_N} = \{\mathbf{v} \in H(\mathrm{div}, \Omega),\ \mathbf{v}_s = \mathbf{v}|_{\Omega_s} \in (H^1(\Omega_s))^3,\ \mathbf{v} \cdot \nu = u_N \text{ on } C, \\ \mathbf{v} \cdot \tau_i = 0 \text{ on } \partial\Omega \cap \partial\Omega_s,\ i = 1, 2\} \end{aligned} \tag{2.11}$$

and

$$W = \begin{cases} L^2(\Omega), & \text{if} \quad C \neq \partial\Omega, \\ L^2(\Omega)/\mathbb{R}, & \text{if} \quad C = \partial\Omega. \end{cases}$$

If $\bar{\mathbf{v}}$ is an arbitrary function in $\bar{\mathbf{V}}$, then $\bar{\mathbf{V}}$ can be written as

$$\bar{\mathbf{V}} = \bar{\mathbf{v}} + \mathbf{V},$$

where $\mathbf{V}$ is the linear space $\mathbf{V} = \bar{\mathbf{V}}_0$. We note that if $C = \partial\Omega$, then the pressure p is only defined up to a constant, and $W = L^2/\mathbb{R}$ is the appropriate function space.

Let $(\cdot,\cdot)$ be the $L^2(\Omega)$ or $(L^2(\Omega))^3$ inner product. Let $(\cdot,\cdot)_l$, $l = s, d$ represent the same, but instead of Ω, the integrals are defined on Ω_l. Let $\langle\cdot,\cdot\rangle_{\mathcal{O}}$ denote the $L^2(\mathcal{O})$ inner product, where $\mathcal{O}$ is a boundary set, i.e., $\mathcal{O}$ represents Γ, $\partial\Omega$, or a subset of $\partial\Omega$. To abbreviate the notation, we also denote $\partial\Omega_l \cap \partial\Omega$ by ∂_l, $l = s, d$.

We multiply both sides of (2.1) by $\mathbf{v} \in \mathbf{V}$ and integrate by parts. The left side of the equation yields

$$\begin{aligned}
&-2\mu(\nabla\cdot D\mathbf{u},\mathbf{v})_s + (\nabla p,\mathbf{v})_s \\
&\qquad = 2\mu(D\mathbf{u},D\mathbf{v})_s - (p,\nabla\cdot\mathbf{v})_s \\
&\qquad\quad - 2\mu\langle\nu\cdot D\mathbf{u}_s,\mathbf{v}\rangle_\Gamma + \langle p_s,\mathbf{v}\cdot\nu\rangle_\Gamma + \langle\nu\cdot(pI-2\mu D\mathbf{u}),\mathbf{v}\rangle_{\partial_s}
\end{aligned}$$

We manipulate the first and last boundary terms and use (2.6), (2.7), (2.9), (2.10) and (2.11) to obtain

$$\begin{aligned}
2\mu\langle\nu\cdot D\mathbf{u}_s,\mathbf{v}\rangle_\Gamma &= 2\mu\langle\nu\cdot D\mathbf{u}_s\cdot\nu,\mathbf{v}\cdot\nu\rangle_\Gamma + 2\mu\sum_i\langle\nu\cdot D\mathbf{u}_s\cdot\tau_i,\mathbf{v}_s\cdot\tau_i\rangle_\Gamma \\
&= \langle p_s-p_d,\mathbf{v}\cdot\nu\rangle_\Gamma - \mu\sum_i\langle\alpha K^{-1/2}\mathbf{u}_s\cdot\tau_i,\mathbf{v}_s\cdot\tau_i\rangle_\Gamma \\
\langle\nu\cdot(pI-2\mu D\mathbf{u}),\mathbf{v}\rangle_{\partial_s} &= \langle\nu\cdot(pI-2\mu D\mathbf{u})\cdot\nu,\mathbf{v}\cdot\nu\rangle_{\partial_s} \\
&\quad + \sum_i\langle\nu\cdot(pI-2\mu D\mathbf{u})\cdot\tau_i,\mathbf{v}\cdot\tau_i\rangle_{\partial_s} \\
&= \langle p_B,\mathbf{v}\cdot\nu\rangle_{\partial_s\backslash C}.
\end{aligned}$$

Then, (2.1) becomes

$$\begin{aligned}
&2\mu(D\mathbf{u},D\mathbf{v})_s - (p,\nabla\cdot\mathbf{v})_s + \mu\sum_i\langle\alpha K^{-1/2}\mathbf{u}_s\cdot\tau_i,\mathbf{v}_s\cdot\tau_i\rangle_\Gamma \\
&\qquad + \langle p_d,\mathbf{v}\cdot\nu\rangle_\Gamma + \langle p_B,\mathbf{v}\cdot\nu\rangle_{\partial_s\backslash C} = (f,\mathbf{v})_s.
\end{aligned} \tag{2.12}$$

Similarly, (2.3) is transformed into

$$\mu(K^{-1}\mathbf{u},\mathbf{v})_d + (\nabla p,\mathbf{v})_d$$
$$= \mu(K^{-1}\mathbf{u},\mathbf{v})_d - (p,\nabla\cdot\mathbf{v})_d - \langle p_d,\mathbf{v}\cdot\nu\rangle_\Gamma + \langle p_B,\mathbf{v}\cdot\nu\rangle_{\partial_d\backslash C} = (f,\mathbf{v})_d \tag{2.13}$$

where we have used that $\mathbf{v}\cdot\nu = 0$ on C and that the unit normal ν on Γ points into Ω_d.

Combining (2.12) and (2.13) we obtain the following variational formulation of problem (2.1)–(2.10), with the solution $(\mathbf{u},p)$ in the space $(\bar{\mathbf{V}},W)$ and test functions $(\mathbf{v},w)\in(\mathbf{V},W)$,

$$2\mu(D\mathbf{u},D\mathbf{v})_s + \mu\sum_i\langle\alpha K^{-1/2}\mathbf{u}_s\cdot\tau_i,\mathbf{v}_s\cdot\tau_i\rangle_\Gamma$$
$$+ \mu(K^{-1}\mathbf{u},\mathbf{v})_d - (p,\nabla\cdot\mathbf{v}) = (f,\mathbf{v}) - \langle p_B,\mathbf{v}\cdot\nu\rangle_{\partial\Omega\backslash C}, \tag{2.14}$$
$$(\nabla\cdot\mathbf{u},\omega) = (g,\omega). \tag{2.15}$$

As we noted above, it can be seen from (2.14)–(2.15) that if $C = \partial\Omega$, p is defined up to a constant and $W = L^2(\Omega)/\mathbb{R}$ is the appropriate space for the pressure.

2.2 Discretization of the differential system

The algebraic linear system that we study in the next Chapter comes from the discretization of system (2.14-2.15) using a mixed finite element method proposed in [4]. In this reference, the authors develop the case when the space dimension $d = 2$. In this section, we briefly review their method in two dimensions and then explain its generalization to the three dimensional case, which we use in our code for the numerical simulations of Chapter 5.

2.2.1 The two dimensional finite elements

The main idea is the use of the standard Stokes finite element space introduced in [7] modified in such a way that discontinuities of the tangential component of the velocity might be present on the Darcy-Stokes interface. The finite element is defined on a rectangle. It is assumed that both Ω_s and Ω_d are unions of rectangles. Therefore each element is either in Ω_s or Ω_d. On each element R, the pressure is approximated by a constant and the velocity $\mathbf{v} = (v_x, v_y)$ is approximated in the space $Q_{1,2}(R) \times Q_{2,1}(R)$, where $Q_{i,j}(R)$ is the space of polynomials on R of degree i in x and degree j in y. For each unmodified element, where no degree of freedom has been removed, we have 12 degrees of freedom for the velocity: 8 values for the velocities at the corners in the x and y directions and 4 edge average fluxes per unit length. Figure 2.1 shows a typical element on rectangle $R = (0, a) \times (0, b)$.

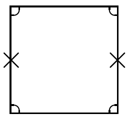

$$v_x(x, y) = (a - x)P_2(y) + x\hat{P}_2(y)$$

Figure 2.1: *Finite element on rectangle $R = (0, a) \times (0, b)$. There are 6 degrees of freedom for the velocity in the x-direction. The general form of a function $v_x \in Q_{1,2}(R)$ is given, where P_2 and $\hat{P}_2$ are second degree polynomials on (0,b).*

The finite element space is obtained in the usual way, by piecing together the functions defined on rectangles with matching degrees of freedom. We then obtain a space of locally polynomial continuous functions on Ω. In order to allow for discontinuity of the tangential velocity across the interface, the elements near the interface should be modified. This is accomplished by removing some degrees of freedom from elements on the Darcy side of the interface. For a discontinuity in the x-velocity, the two cases where this applies are shown in Figure 2.2. A quarter circle indicates that the degree of freedom at the corner is preserved and the absence of it indicates that it has been removed. As the figure shows, the degrees of freedom corresponding to the tangential velocity on the Darcy side of the interface have been removed.

Figure 2.2: *Modified elements to allow for discontinuity in the tangential x-velocity across the interface. d represents a Darcy element and s a Stokes element. The heavy line corresponds to the interface. Degrees of freedom at the corner are removed from elements on the Darcy side of the interface.*

The removal of degrees of freedom implies a reduction in the degree of the approximating polynomials.

It is shown in [4] that this method gives global first order convergence in the L^2 norm for the velocity and the pressure and for the gradient of the velocity in the Stokes domain. A lower dimension modification is also introduced, where degrees of freedom are removed at the corners of all the elements in the Darcy domain which are away from the interface. Thus, the elements on the Darcy region that are not near the interface become Raviart-Thomas elements [24, 14]. The authors investigated the convergence properties of this lower dimension method numerically and observed the same order of convergence that they were able to prove for the higher dimension method. Since we were interested in doing computations with larger systems in three dimensions, and the computing time was an important factor for us, we decided to use this lower dimension modification in our computations.

2.2.2 The three dimensional finite elements

We now give the three dimensional generalization of the finite element method explained above. Let $R = (-a, a) \times (-b, b) \times (-c, c)$ be a reference rectangle in $\mathbb{R}^3$. Let $Q_{i,j,k}(R)$ be the space of polynomials defined on R of degree i in x, j in y and k in z. Let $B_x(R)$ be the space of polynomials p on R of the form

$$B_x(R) = \{p(x, y, z) = (y - b)(y + b)(z - c)(z + c)P_1(x)\},$$

where $P_1(x)$ is a polynomial on $(-a, a)$ of degree 1. Similarly, we define $B_y(R)$ and $B_z(R)$. The functions of these spaces are called *bubble* functions.

On each unmodified element (no degree of freedom removed), the pressure is approximated by a constant and the velocity is approximated in the space

$$\mathbf{V}_R = (Q_{1,1,1}(R))^3 + B_x(R) \times B_y(R) \times B_z(R).$$

We have 10 degrees of freedom for each direction: 8 values for the velocity at the corners of the three dimensional rectangle and 2 values for the face average flux per unit area through the faces perpendicular to that direction. For example, if we consider the cube $R = (-1, 1) \times (-1, 1) \times (-1, 1)$ as the reference element, then the function $\mathbf{v}_c = (v_c, 0, 0)$,

$$v_c(x, y, z) = \frac{1}{8}(x + 1)(y + 1)(z + 1) - \frac{9}{32}(x + 1)(y^2 - 1)(z^2 - 1),$$

is the function in $\bar{V}_R$ with all degrees of freedom equal to 0 except for its value at corner $(1,1,1)$, which is 1. Similarly $\mathbf{v}_b = (v_b, 0, 0)$,

$$v_b(x,y,z) = \frac{9}{8}(x+1)(y^2-1)(z^2-1),$$

is the bubble function whose average flux per unit area through face $x = 1$ is 1 and the rest of its degrees of freedom are equal to 0.

As for the modification of the elements, we already mentioned that for the purposes of our computations, we chose to use Raviart-Thomas elements in the Darcy subdomain away from the interface Γ. Near Γ, we want to remove as many degrees of freedom as possible. In order to achieve this, we start with no corners at all on Darcy elements. Since we must not remove corners from Stokes elements, our procedure is to add corners to a Darcy element only when it is necessary to preserve the continuity of the normal flux through a face that is shared by such element and a Stokes element.

2.2.3 The finite element method

Let us assume now that $\Omega \subset \mathbb{R}^3$ and that both Ω_s and Ω_d are unions of rectangles. Let $\mathcal{T}_h$ be a rectangular, conforming finite element partition of Ω with mesh size h. We define our finite element space in the usual way. Let $W_h \subset W$ be the set of piecewise constant functions over $\mathcal{T}_h$, and let $\bar{\mathbf{V}}_h'$ be the set of continuous functions $\mathbf{v} \in \bar{\mathbf{V}}$ such that the restriction $\mathbf{v}|_R \in \mathbf{V}_R$ for all rectangles $R \in \mathcal{T}_h$. Similarly, let $\mathbf{V'}_h = \{\mathbf{v} \in \mathbf{V} \cap C(\Omega) : \mathbf{v}|_R \in \mathbf{V}_R \text{ for all } R \in \mathcal{T}_h\}$. The functions in $\bar{\mathbf{V}}_h'$ and $\mathbf{V'}_h$ are obtained by piecing together the polynomial functions defined on each rectangle, with matching degrees of freedom at corners and faces. Since we modify the elements to allow for discontinuities in the tangential velocity at the interface, we need to modify the spaces $\bar{\mathbf{V}}'_h$ and $\mathbf{V}'_h$ accordingly. Let $\bar{\mathbf{V}}_h$ and $\mathbf{V}_h$ be the respective modified finite element spaces.

Now we can formulate the discrete version of (2.14)–(2.15). We search for the pair $(\mathbf{u}_h, p_h) \in (\bar{\mathbf{V}}_h, W_h)$ such that, for all functions $(\mathbf{v}_h, \omega_h)$ in a basis of $(\mathbf{V}_h, W_h)$, we have

$$\begin{aligned} 2\mu(D\mathbf{u}_h, D\mathbf{v}_h)_s &+ \mu\sum_i \langle \alpha K^{-1/2}\mathbf{u}_{h,s}\cdot\tau_i, \mathbf{v}_{h,s}\cdot\tau_i\rangle_\Gamma \\ &+ \mu(K^{-1}\mathbf{u}_h, \mathbf{v}_h)_d - (p_h, \nabla\cdot\mathbf{v}_h) = (f, \mathbf{v}_h) - \langle p_B, \mathbf{v}_h\cdot\nu\rangle_{\partial\Omega\setminus C}, \end{aligned} \tag{2.16}$$

$$(\nabla\cdot\mathbf{u}_h, \omega_h) = (g, \omega_h). \tag{2.17}$$

2.3 Convergence of the finite element method

As we mentioned above, an optimal order convergence result for the two dimensional version of (2.16)–(2.17) was proved in [4]. All the arguments can be readily extended to the three dimensional case, and we have the following theorem. For the notation, $\|\cdot\|_{m,l}$ denotes the usual norm in the Sobolev space $H^m(\Omega_l)$, for $m = 1, 2$ and $l = s, d$, and $\|\cdot\|_{0,l}$ is the $L^2(\Omega_l)$ norm. Also, $\mathcal{P}_{\mathcal{W}} : L^2(\Omega) \to W_h$ denotes the L^2 projection operator.

Theorem 2.3.1. *Assume that the solution* $(\mathbf{u}, p)$ *of* (2.14)–(2.15) *is sufficiently smooth so that all the norms that appear below are finite. Then, there is a constant* C *such that*

$$\begin{aligned} &\|\mathbf{u}-\mathbf{u}_h\|_{1,s} + \|\mathbf{u}-\mathbf{u}_h\|_{0,d} + \|p-p_h\|_0 \\ &\qquad \le Ch(\|f\|_{1,d} + \|\mathbf{u}\|_{2,s} + \|\mathbf{u}\|_{1,d} + \|p\|_{1,s} + \|p\|_{1,d} + \|p_d\|_{1,\Gamma}). \end{aligned} \tag{2.18}$$

Moreover, $\mathcal{P}_{\mathcal{W}}\nabla\cdot\mathbf{u}_h = \mathcal{P}_{\mathcal{W}}g$.

Chapter 3

A Multigrid Solver for the Discretized System

3.1 Introduction

Our goal is to develop a solver for the linear system

$$\begin{bmatrix} A & B \\ B^t & 0 \end{bmatrix} \begin{bmatrix} u \\ p \end{bmatrix} = \begin{bmatrix} f \\ g \end{bmatrix} \tag{3.1}$$

for a velocity u and a pressure p, which corresponds to boundary value problem (2.14)–(2.15) that has been discretized using the finite element method (2.16)–(2.17) described in the previous chapter. Here, A is a matrix of size $n \times n$ and B has size $n \times m$, with $n > m$.

Without loss of generality, we assume that the function u_N in (2.8) is identically zero, so that $\bar{\mathbf{V}} = \mathbf{V}$. (Otherwise we write the unknown $\mathbf{u}$ as $\mathbf{u} = \bar{\mathbf{u}} + \bar{\bar{\mathbf{u}}}$, where $\bar{\mathbf{u}}$ is any known function in $\bar{\mathbf{V}}$ and $\bar{\bar{\mathbf{u}}} \in \mathbf{V}$, and rewrite system (2.14)–(2.15) in terms of the new unknown $\bar{\bar{\mathbf{u}}}$ by passing those terms containing $\bar{\mathbf{u}}$ to the right hand side). We also assume that $C \neq \partial\Omega$. We will return to the case $C = \partial\Omega$ in Section 3.4. For clarity of the exposition, we assume that $\Omega \subset \mathbb{R}^d$, with $d = 2$, but our method can be easily generalized to dimension $d = 3$. In fact, all the computations that we present in Chapters 5 and 6 use the three dimensional version of our solver. Also, to simplify the notation and the diagrams, we use square elements throughout this chapter, the generalization to general rectangular elements being obvious.

Since the vugs and the matrix rock are intertwined and have very different flow properties, there are large jumps in the elements of the matrix A and the resulting system is ill-conditioned (as we will see in Table 3.1 below). Matrix coefficients for system (3.1) are given by

$$\begin{aligned} A_{i,j} &= 2\mu(D\mathbf{v}^j, D\mathbf{v}^i)_s + \mu(\alpha K^{-1/2}\mathbf{v}_s^j \cdot \tau, \mathbf{v}_s^i \cdot \tau)_\Gamma + \mu(K^{-1}\mathbf{v}^j, \mathbf{v}^i)_d, \qquad (3.2)\\ B_{i,j} &= -(\nabla \cdot \mathbf{v}^i, \omega_j),\\ f_i &= (f, \mathbf{v}^i) - \langle p_B, \mathbf{v}^i \cdot \nu\rangle_{\partial\Omega\setminus C},\\ g_i &= (g, \omega^i), \end{aligned}$$

where the $\mathbf{v}^i$ and ω^i are velocity and pressure basis functions, respectively. Note that for a specific coefficient A_{ij}, some of the three terms that appear in (3.2) might be zero. A rough estimate of the order of magnitude of those terms is given as follows.

First, in the cgs unit system, $\mu \approx 10^{-2}$, $\alpha \approx 1$ and $K \approx 10^{-10}$. If h is the mesh size, and it approximately represents the diameter of a vug, then $h \sim 1$, say. Thus, in dimension d,

$$\begin{aligned} \mu(D\mathbf{v}^j, D\mathbf{v}^i)_s &\sim \mu h^{d-2} \sim 10^{-2},\\ \mu(\alpha K^{-1/2}\mathbf{v}_s^j \cdot \tau, \mathbf{v}_s^i \cdot \tau)_\Gamma &\sim \mu\alpha h^{d-1}K^{-1/2} \sim 10^3,\\ \mu(K^{-1}\mathbf{v}^j, \mathbf{v}^i)_d &\sim \mu h^d K^{-1} \sim 10^8, \end{aligned}$$

which explains the large jumps in the coefficients of A.

The condition number of matrix A for different systems is shown in Table 3.1. The domain is 8 cm × 8 cm × 4 cm and the mesh size is $h = 1$

Type of system	Matrix size	Condition number
Darcy homogeneous	896 × 896	9.9124e+03
Darcy heterogeneous	896 × 896	8.3731e+05
Stokes only	615 × 615	2.1497e+07
Darcy-Stokes (isolated vug)	968 × 968	3.7116e+11
Darcy-Stokes (connected vug)	998 × 998	6.8248e+11

Table 3.1: *Condition number of matrix A for different systems. Darcy-Stokes systems are very ill-conditioned.*

cm. We include five cases: (1) a Darcy domain with uniform permeability of 1 md, (2) a heterogeneous Darcy domain with a permeability variation of 4 orders of magnitude, (3) a Stokes domain (using a 4 cm cube domain), (4) a Darcy-Stokes system with a heterogeneous Darcy subdomain with an isolated vug, and (5) a Darcy-Stokes system with a heterogeneous Darcy subdomain and a connected vug. Notice the large condition number of matrix A for vuggy systems, and how much larger it is than for both simply heterogeneous porous media and pure Stokes systems.

In [4], the authors use an Uzawa algorithm to solve system (3.1). Such an ill-conditioned system requires a good preconditioner in order for an iterative method to converge at a reasonable rate. They note that A has a block structure induced by the x and y components of the velocity, and approximate the inverse A^{-1} by

$$A^{-1} \sim \begin{pmatrix} A_{xx}^{-1} & 0 \\ 0 & A_{yy}^{-1} \end{pmatrix},$$

that is, they omit $A_{xy} = A_{yx}$. This preconditioner turned out to be very effective, but quite expensive to compute. Because of the large computing time required for systems larger than about 128×128, the method was not very useful in practice, and not suitable for three dimensions. The use of a simpler preconditioner considerably reduces the rate of convergence due to the fact that low frequency components of the error are not efficiently removed during the iterative procedure.

This was our motivation to design a multigrid solver for system (3.1). It is well known, however, that developing a multigrid method for a system with highly oscillating coefficients also poses serious challenges since the lack of regularity of the solution makes it difficult to define prolongation and restriction operators. Operator-dependent interpolation has been proposed for the diffusion equation with jumping coefficients [2, 30], where a discontinuity of the coefficients implies a discontinuity in the gradient of the solution, but the product of these two terms should be continuous. The prolongation operator is designed to preserve the continuity of this product. In this case, the equation changes from one point to another in the domain only by the jumping coefficient. Our case is more complicated, because the differential operator is totally different in the Darcy and Stokes subdomains. Another tool used to deal with varying coefficients is algebraic multigrid [25, 28], in which geometric grids are not considered at all. The starting point is the linear system and all the arguments come from the analysis of the matrix structure. We did not follow this approach because of the physical nature of our problem. As it is explained in Section (3.4), our definition of the prolongation operator is based on an interpretation of coarse grid quantities as average fluxes on coarse grid edges, the use of mass conservation, and the analysis of the relative order of magnitude of the flux in the Darcy and Stokes subdomains.

3.2 Review of multigrid

For a detailed treatment of multigrid methods, we refer the reader to [30, 12, 18]. Here we present the main ideas. Suppose we want to solve the system

$$L_h x = b, \tag{3.3}$$

where matrix L_h represents the discretized version of a partial differential operator with certain boundary conditions, and x and b are functions defined on a certain grid G_h with mesh size h.

We could try to solve this system using an iterative method. Most of these methods efficiently reduce the high frequency components of the error $x - x^n$, where x^n is the approximation to x obtained after the n iteration. However, they do not remove the low frequency components. If we try to solve (3.3) using such a smoothing procedure, we will observe that after a number of iterations, the reduction in the magnitude of the error becomes very small. In order to overcome this difficulty, we need a better method to eliminate the slow components of the error.

We observe that the notion of high frequency or low frequency for a function defined on a grid depends on the mesh size. A grid function which is 'slow' relative to a grid with mesh size h becomes a relatively faster signal when restricted to a subgrid with mesh size $2h$. This idea is illustrated in Figure 3.1. Notice that the phase change of the sinusoidal function from one grid point to the next is larger when the function is restricted to the coarser grid.

Suppose now that we apply a number of smoothing iterations and obtain an approximation x_h to the exact solution x of (3.3). If y solves the

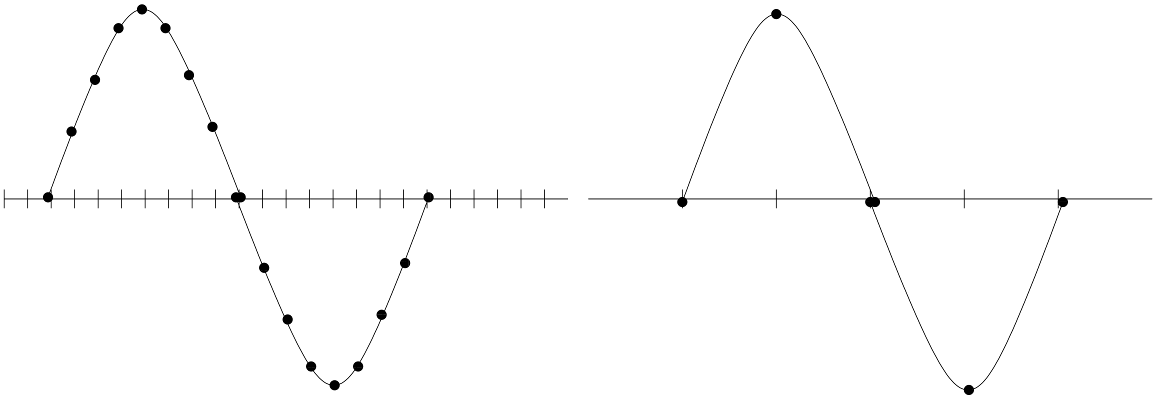

Figure 3.1: *A discrete signal becomes more rapidly oscillating when restricted to a coarser grid.*

residual equation

$$L_h y = r_h = b - L_h x_h, \tag{3.4}$$

then $x_h + y = x$ is the exact solution of (3.3). We also know that high frequency components have been removed from the error $x - x_h$, so $y = x - x_h$ should basically contain slow components (relative to grid G_h). Then, we try to 'solve' Equation 3.4 on a coarser grid with mesh size, say, $2h$. Let G_{2h} be such a grid. We need to define some version of the operator L_h for grid G_{2h}. Denote this new operator by L_{2h}. We also need to define the right hand side for the new equation. To this end we define a restriction operator R_h^{2h}. The residual equation posed on grid G_{2h} reads

$$L_{2h} y_{2h} = R_h^{2h} r_h, \tag{3.5}$$

where the unknown y_{2h} is obviously a function defined on grid G_{2h}.

Once we solve (3.5) we need to add this coarse-grid correction to x_h, but first, we need to prolongate y_{2h} to a function defined on G_h, so we define a prolongation operator P_{2h}^h. We then obtain a better approximation to x given by

$$x_h + P_{2h}^h y_{2h}.$$

When we add the coarse-grid correction $P_{2h}^h y_{2h}$ to x_h, we also introduce high frequency components to the error $x - x_h$. Therefore, at this point we need to apply a number of smoothing iterations. This is called post-smoothing, in contrast to the pre-smoothing applied to system (3.3) before solving the residual equation (3.4). Pre-smoothing is stopped when it becomes inefficient to decrease the magnitude of the residual. Then we solve (3.4), add the coarse-grid correction and apply post-smoothing.

It turns out that we do not need to solve (3.5) exactly, we just need an approximate solution. Therefore we can now follow the same steps we did before: we first apply a number of smoothing iterations on G_{2h} and then we solve the residual equation on G_{4h} and so on, until we reach a sufficiently coarse grid, where an exact solver can be applied inexpensively.

The process that we have just described can be represented graphically as in Figure 3.2. Each horizontal level corresponds to a particular mesh size, or equivalently, to a particular grid. We move from left to right in the diagram as the multigrid algorithm runs. Each dot represents an application of the smoothing procedure. If we are descending, we perform pre-smoothing operations and restrict the residual equation to the immediately coarser grid. If we are ascending, the solution of the residual equation is prolongated and added to the existing approximation at the immediately finer grid, and post-smoothing operations are performed. The vertex of the V corresponds to the coarsest grid, where the residual equation is solved exactly. This type of scheme is called a V-cycle, because of the shape of the diagram, and each V represents one multigrid iteration. There are other choices, for example, a W-cycle is shown in Figure 3.3. Also, there are different types of W-cycles.

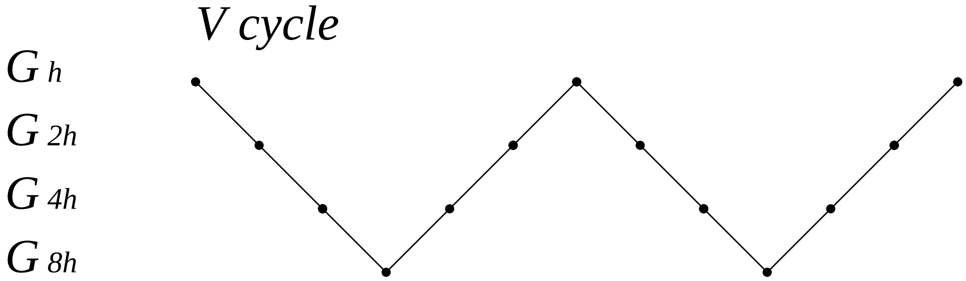

Figure 3.2: *Schematic representation of a multigrid algorithm. Each dot represents the application of a number of smoothing iterations on a particular grid level. The lines connecting the dots represent the restriction of the residual equation to the immediately coarser grid if we move downwards, and the prolongation of the coarse-grid correction to the immediately finer grid, if we move upwards.*

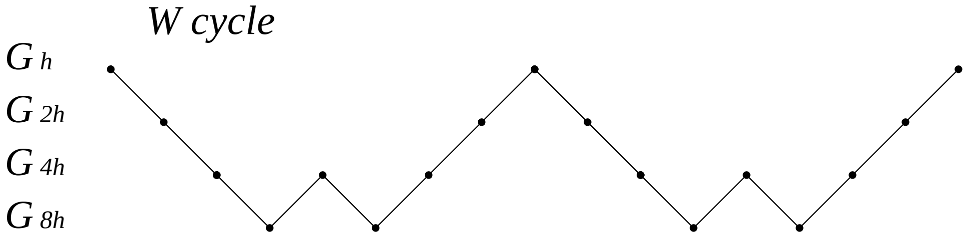

Figure 3.3: *In a W-cycle , more than one iteration is performed on some coarse grids before we move to finer grids.*

According to the discussion above, in order to design a multigrid algorithm we need to specify: (1) the type of cycle, (2) the grid coarsening strategy, (3) the coarse grid operators, (4) the smoothing procedure and (5) the intergrid transfer operators (restriction and prolongation operators). We will now explain our choices. The most important aspect is choosing the smoother and prolongation and restriction operators.

3.3 An effective multigrid method for the Darcy-Stokes system

For the type of cycle we use, our algorithm performs V-cycles. We found a better balance between convergence rate and computational work for these types of schemes than for W-cycles.

3.3.1 Coarsening strategy

Let G^M denote the finest grid. Actually, G^M denotes the nodal points where the solution $(u, p) = (u_x, u_y, p)$ of (3.1) is defined (see Figure 3.4). Then $G^M = G_x^M \cup G_y^M \cup G_p^M$, where G_x^M, G_y^M, G_p^M are subgrids of G^M where u_x, u_y and p are respectively defined. (Although the degrees of freedom corresponding to the fluxes are defined on edges, we will identify an edge with its midpoint as the figure shows. Also, we identify each cell where the pressure is defined with its center point). We assume that G^M has mesh size h. Then G_x^M consists of the corner points $\{(ih, jh)\}$ and the edge points $\{(ih, (j + 1/2)h)\}$. Similarly, G_y^M contains $\{(ih, jh)\}$ and $\{((i+1/2)h, jh)\}$ and G_p^M is $\{((i+1/2)h, (j+\frac{1}{2})h)\}$.

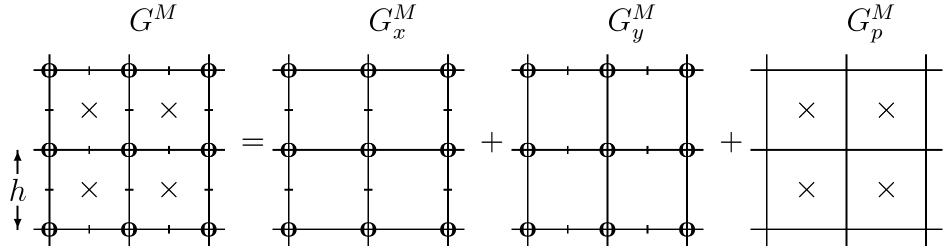

Figure 3.4: *Finest grid* $G^M = G_x^M \cup G_y^M \cup G_p^M$. *Velocities in the x and y direction are defined at corners of elements. Average unit fluxes are defined on edges. Pressure is constant on each element.*

Let $G^{M-1}, ..., G^0$ denote a sequence of successively coarser grids constructed from G^M as follows. G^{M-1} is obtained from G^M by removing the corner points, so G^{M-1} also has mesh size h. We also have $G^{M-1} = G_x^{M-1} \cup G_y^{M-1} \cup G_p^{M-1}$, where G_x^{M-1} and G_y^{M-1} are obtained from G_x^M and G_y^M respectively by removing the corners and $G_p^{M-1} = G_p^M$. Given grid G^k, $k = M-1, M-2, ..., 1$, each cell of grid G^{k-1} consists of 4 neighboring cells of grid G^k, so we coarsen the grid by doubling the mesh size. In the same way we had for G^k, for each cell of G^{k-1} we have a grid point at the center of the cell where 'pressure' will be defined and the midpoint of each edge where 'fluxes' will be defined (Figure 3.5). For every $k = M, M-1, .., 0$ we have $G^k = G_x^k \cup G_y^k \cup G_p^k$, where the definitions of these non-nested subgrids of G^k are now obvious from the previous discussion. That is, for $k < M$, $h_k = 2^{M-k-1}h$ and G_x^k is $\{(ih_k, (j+1/2)h_k)\}$, G_y^k is $\{((i+1/2)h_k, jh_k)\}$ and G_p^k is $\{((i+1/2)h_k, (j+1/2)h_k)\}$

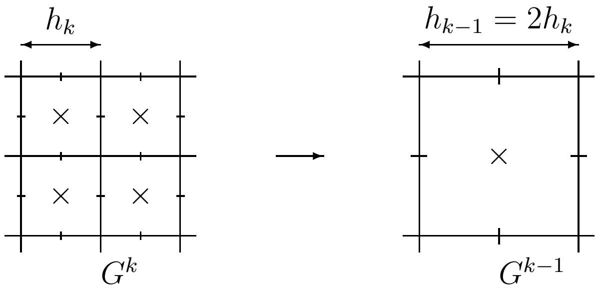

Figure 3.5: *Grid coarsening for* $k = M-1, M-2, ..., 1$.

Notice that this coarsening strategy preserves the cell structure of the finest grid (except for the corners), which allows us to think of the unknown quantities defined on coarser grids as cell pressures and edge average fluxes per unit length. This way of thinking will guide us in the design of the prolongation and restriction operators.

3.3.2 Coarse-grid operators

We need to define the analog of (3.1) for each grid. One possible choice is to consider the finite element space associated to the corresponding elements or cells. However, it has the serious disadvantage that the functions of these finite element spaces are continuous in the interior of every element. A discontinuity on a segment of the Darcy-Stokes interface contained in the interior of an element would not be allowed on coarser grids. Therefore, we will use the so called Galerkin coarse grid approximation, where the discrete operator for level k is recursively given by

$$L_k = R_{k+1}^k L_{k+1} P_k^{k+1}, \quad k = M-1, M-2, ..., 0, \tag{3.6}$$

where L_M is given by (3.1), P_k^{k+1} is the prolongation operator that takes grid functions defined on G^k into grid functions defined on G^{k+1} and R_{k+1}^k is the restriction operator acting in the opposite direction. To maintain symmetry, we choose R_{k+1}^k to be $(P_k^{k+1})^t$. After suitably defining the prolongation operator in the next section, it will be easy to prove that for each $k = M, M-1, ..., 0$, L_k has the form

$$L_k = \begin{bmatrix} A^k & B^k \\ (B^k)^t & 0 \end{bmatrix}, \tag{3.7}$$

where A^k is symmetric and positive definite. We will also prove that L_k satisfies the inf-sup condition, and therefore the system

$$L_k x_k = b_k \tag{3.8}$$

has a unique solution for any grid function b_k on G^k.

3.3.3 Smoothing procedure

The difficulty in finding a good smoother for (3.1) is that the system, as we saw earlier, is extremely ill-conditioned. We present here a new smoother that has worked well for our problem. In order to abbreviate the notation we explain the smoothing procedure for the finest grid. Because of (3.7), everything is valid for coarser grids, except for minor differences that we will mention below.

Suppose we have computed an approximation (u^n, p^n) to the solution (u, p) of system (3.1), and we want to compute a better approximation (u^{n+1}, p^{n+1}) by smoothing the error. The first step of our method is to find the *directions* along which we should modify (u^n, p^n). In other words, we try to find *optimal* vectors du and dp to define (u^{n+1}, p^{n+1}) as

$$\begin{aligned} u^{n+1} &= u^n + \beta\, du, \\ p^{n+1} &= p^n + \alpha\, dp, \end{aligned} \tag{3.9}$$

for appropriate values of α and β that will be determined in the second step of our procedure.

If du and dp are "good directions," it is reasonable that they should approximate the errors $e_u = u - u^n$ and $e_p = p - p^n$, and therefore can be obtained by computing an approximate solution of

$$\begin{bmatrix} A & B \\ B^t & 0 \end{bmatrix} \begin{bmatrix} e_u \\ e_p \end{bmatrix} = \begin{bmatrix} r^n \\ s^n \end{bmatrix}, \tag{3.10}$$

where r^n and s^n are the residuals

$$\begin{aligned} r^n &= f - Au^n - Bp^n, \\ s^n &= g - B^t u^n. \end{aligned}$$

We obtain an approximate solution of (3.10) using the Uzawa algorithm [10, 11]. Let $\widehat{A} = diag(A)$, i.e., $\widehat{A}$ is diagonal and $\widehat{A}_{ii} = A_{ii}$ for all indexes i, and let C^{-1} be a preconditioner for $B^tA^{-1}B$, such as $C = diag(B^t\widehat{A}^{-1}B)$ (we return to this choice near the end of this subsection). Then Uzawa iterations (indexed by l) are given by

$$e_u^{l+1} = e_u^l + a\widehat{A}^{-1}(r^n - Ae_u^l - Be_p^l), \tag{3.11a}$$

$$e_p^{l+1} = e_p^l + bC^{-1}(B^te_u^{l+1} - s^n), \tag{3.11b}$$

where $a, b > 0$ are damping parameters. We generally obtained good results with $a = b$ between 0.4 and 0.8.

We make a parenthesis here to give an intuitive explanation of the Uzawa algorithm. For this, we rewrite (3.10), dropping index n to simplify the notation, as

$$Ae_u = r - Be_p, \tag{3.12a}$$

$$B^te_u = s. \tag{3.12b}$$

Equation (3.11a) is relatively clear, since $\widehat{A}^{-1}$ is a preconditioner for A. This then has the general form of an iterative method: the new approximation is the old approximation plus the residual multiplied by a preconditioner. Equation (3.11b) is less obvious. If (e_u^{l+1}, e_p^l) is the best approximation of (e_u, e_p) that we have at the moment, we can write

$$e_u^{l+1} \approx A^{-1}(r - Be_p^l),$$

and so

$$B^te_u^{l+1} \approx B^tA^{-1}r - B^tA^{-1}Be_p^l. \tag{3.13}$$

On the other hand, multiplying (3.12a) by B^tA^{-1}, we have

$$B^tA^{-1}Be_p = B^tA^{-1}r - B^te_u = B^tA^{-1}r - s. \tag{3.14}$$

From (3.14), we can define e_p^{l+1} using the general scheme of an iterative method:

$$e_p^{l+1} = e_p^l + C^{-1}(B^t A^{-1} r - s - B^t A^{-1} B e_p^l), \tag{3.15}$$

where C^{-1} was defined above as a preconditioner that approximates the inverse of $B^t A^{-1} B$. Now using (3.13), we obtain

$$e_p^{l+1} = e_p^l + C^{-1}(B^t e_u^{l+1} - s). \tag{3.16}$$

In fact, if $\widehat{A}^{-1}$ and C^{-1} were exact preconditioners, the scheme would converge immediately.

Returning to our method, we perform a number of Uzawa iterations given by (3.11) starting with $e_u^0 = e_p^0 = 0$ to compute the direction quantities du and dp, i.e., we set

$$du = e_u^L \quad \text{and} \quad dp = e_p^L$$

for some L. The value for L is problem dependent. We obtained good results with L between 5 and 40 for the problems we solved.

Once we have computed du and dp, the second step consists of finding optimal values for α and β in (3.9). We search for the values of α and β that minimize the residual corresponding to the $(n+1)st$ iteration. More precisely, let

$$\begin{aligned} r^{n+1} &= f - Au^{n+1} - Bp^{n+1}, \\ s^{n+1} &= g - B^t u^{n+1}. \end{aligned}$$

Then, we try to minimize $R = w_u |r^{n+1}|^2 + w_p |s^{n+1}|^2$, where $|\cdot|$ is the l_2 norm of a vector, and w_u and w_p are weights used to normalize the residuals,

$$w_u = \frac{1}{1 + |u^n|} \quad \text{and} \quad w_p = \frac{1}{1 + |p^n|}.$$

Notice that (3.9) implies

$$r^{n+1} = r^n - \alpha B\,dp - \beta A\,du,$$

$$s^{n+1} = s^n - \beta B^t du,$$

so α and β will be the solutions of the pair of equations

$$w_u(r^n - \alpha B\,dp - \beta A\,du) \cdot B\,dp = 0, \tag{3.17a}$$

$$w_u(r^n - \alpha B\,dp - \beta A\,du) \cdot A\,du + w_p(s^n - \beta B^t du) \cdot B^t du = 0. \tag{3.17b}$$

Rearranging terms in (3.17), we obtain

$$|B\,dp|^2\alpha + B\,dp \cdot A\,du\,\beta = r^n \cdot B\,dp, \tag{3.18a}$$

$$(B\,dp \cdot A\,du)\alpha + (|A\,du|^2 + \frac{w_p}{w_u}|B^t du|^2)\beta = r^n \cdot A\,du + \frac{w_p}{w_u}s^n \cdot B^t du. \tag{3.18b}$$

Notice that the determinant of the matrix for system (3.18) is

$$det = \frac{w_p}{w_u}|B\,dp|^2|B^t du|^2 > 0.$$

We then obtain α and β, which are given by

$$\begin{aligned}\alpha = \Bigg\{ & \left(\frac{w_p}{w_u}|B^t du|^2 + |A\,du|^2\right) r^n \cdot B\,dp \\ & - (A\,du \cdot B\,dp)(r^n \cdot A\,du + \frac{w_p}{w_u}s^n \cdot B^t\,du)\Bigg\}/det,\end{aligned} \tag{3.19a}$$

$$\begin{aligned}\beta = \Bigg\{ & - (B\,dp \cdot A\,du)(r^n \cdot B\,dp) \\ & + |B\,dp|^2(r^n \cdot A\,du + \frac{w_p}{w_u}s^n \cdot B^t du)\Bigg\}/det.\end{aligned} \tag{3.19b}$$

We summarize our smoothing procedure. Given an approximation (u^n, p^n), we first find directions du and dp by running a few Uzawa iterations for system (3.10). Then we compute α and β using formula (3.19), and finally we define (u^{n+1}, p^{n+1}) as given by (3.9).

We suggested above an extremely simple diagonal preconditioner $C^{-1} = (diag(B^t\widehat{A}^{-1}B))^{-1}$ for $B^tA^{-1}B$, which is efficient to apply but not very effective for our highly ill-conditioned system. We can improve this preconditioner by applying it in a Jacobi type iteration. That is, when we wish to solve $B^tA^{-1}Bv = w$ for v, we compute it from several iterations (generally from 5 to 40) of

$$v^{\ell+1} = v^{\ell} + (diag(B^t\widehat{A}^{-1}B))^{-1}(w - B^t\widehat{A}^{-1}Bv^{\ell}), \tag{3.20}$$

which is still quite efficient, since we use $\widehat{A}$ in place of A. That is, we use $(diag(B^t\widehat{A}^{-1}B))^{-1}$ to precondition $B^t\widehat{A}^{-1}B$ in a Jacobi iteration.

Regular Uzawa may sometimes not smooth our Darcy-Stokes system when either the original or modified preconditioner for $B^tA^{-1}B$ is used. However, our two step Uzawa procedure is much more robust. It sometimes smooths when $C = diag(B^t\widehat{A}^{-1}B)$, and generally always smooths (for appropriate choices of parameters) when the Jacobi type C^{-1} is used. That is, our two step Uzawa procedure is valuable when we do not have a very good preconditioner for $B^tA^{-1}B$, which is necessarily true for the three dimensional Darcy-Stokes system.

As we mentioned above, because the coarser grid systems have also a saddle point structure (see (3.7)), our smoothing method is valid for every grid. The analogue of (3.11) is obtained by changing A by A^k and B by B^k. However, for the sake of efficiency, we apply the following minor modifications in the preconditioners, since it is inefficient to compute the diagonal of A^k for each level. If $k < M$ is the grid level, instead of using $\widehat{A^k}^{-1}$ as the preconditioner in the analogue of (3.11a), where $\widehat{A^k} = diag(A^k)$, we use

$$\widehat{\widehat{A^k}}^{-1} = \begin{pmatrix} m_x^{-1}I & 0 & 0 \\ 0 & m_y^{-1}I & 0 \\ 0 & 0 & m_z^{-1}I \end{pmatrix},$$

where, if we let $\widehat{A_x^k}$ be the block of $\widehat{A^k}$ corresponding to degrees of freedom in the x-direction, then

$$m_x = \max_i |\widehat{A_{xii}}|,$$

and similarly for the other blocks. Furthermore, in the analogue of (3.11b), when preconditioning $(B^k)^t(A^k)^{-1}B^k$ by $(C^k)^{-1}$, we do *not* use the preconditioner $(diag((B^k)^t\widehat{A^k}^{-1}B^k))^{-1}$ in (3.20). Instead, we use $(diag((B^k)^t\widehat{\widehat{A^k}}^{-1}B^k)^{-1}$.

At every grid level, we stop performing smoothing iterations after we have performed at least a few (such as 4) iterations and when either the smoothing rate, given by the ratio between the l_2 norms of the residuals corresponding to two consecutive iterations, becomes larger than a prefixed value, or the norm of the residual becomes small enough. In our cases, the tolerance for the smoothing rate was 0.98 and the error tolerance for the residual norm was approximately 10^{-2}. As we explained in Section 3.2, when we stop the pre-smoothing , we move to the immediately coarser grid to find an approximate solution of the residual equation. When we stop post-smoothing, we prolongate our solution to the immediately finer grid and add it to the approximate solution that we have at this level.

3.3.4 Intergrid transfer operators

In our construction, the restriction operator R_k^{k-1} is taken to be the adjoint of the prolongation P_{k-1}^k. This will ensure that the operators L_k, $k = M -$

$1, M, \ldots, 0$, are symmetric and have the same structure as the operator for the finest grid.

The correct design of the prolongation operators turns out to be an important factor in order to obtain a convergent multigrid algorithm. As we mentioned above, the difficulty is due to the fact that the matrix A of system (3.1) has rapidly oscillating coefficients, which implies that the velocity field is also highly oscillating, with jumps of several orders of magnitude between the velocities (or fluxes) on the Darcy and Stokes subdomains. Consequently, the usual transfer operators based on polynomial interpolation fail here.

From a physical point of view, the problem is that the medium contains vug channels that support very high flow rates. This makes prolongation difficult. In order to gain some insight about the orders of magnitude of the velocity on the Stokes and Darcy subdomains, we look at the following simple model case: Consider a Darcy-Stokes system that consists of a channel of width l limited above and below by a porous medium (see Figure 3.6). The flow in the channel satisfies Stokes equation and the flow in the porous medium obeys Darcy's law.

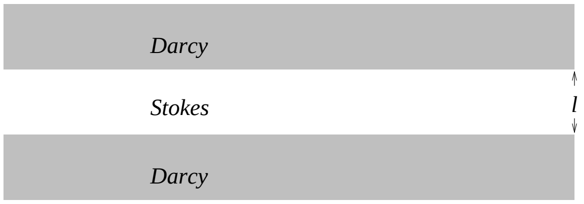

Figure 3.6: *Simple model case of a Darcy-Stokes system with a central channel limited by porous rock.*

We assume that we have a negative unit constant pressure gradient in the x-direction, that the flow is stationary and that the channel is infinitely long in the x-direction, so that the velocity field does not depend on the x-coordinate. (Although the action of the prolongation operator we are trying to construct is local, these assumptions and our model case will prove useful for our purposes.) Let $u(y)$ denote the velocity of the fluid in the x-direction. The Stokes equation for the velocity field in the channel and the Beavers-Joseph-Saffman boundary condition take the simplified form

$$-\mu u''(y) - 1 = 0, \tag{3.21a}$$

$$u'(0) = \alpha K^{-1/2} u(0), \tag{3.21b}$$

$$u'(l) = -\alpha K^{-1/2} u(l). \tag{3.21c}$$

Thus

$$u(y) = -\frac{1}{2\mu} y^2 + by + c,$$

and the boundary conditions imply

$$b = \frac{l}{2\mu} \quad \text{and} \quad c = \frac{lK^{1/2}}{2\mu\alpha}.$$

The average flux per unit length in the channel is $\frac{1}{l}\int_0^l u(y)dy = \frac{lK^{1/2}}{2\mu\alpha} + \frac{l^2}{12\mu}$ and the velocity on the interface is $u(0) = u(l) = \frac{lK^{1/2}}{2\mu\alpha}$. On the other hand, Darcy's law implies that the flux per unit length in the porous medium is $u_d = \frac{K}{\mu}$.

Normally $\alpha \approx 1$. For $K \approx 10^{-10}$ and $l \approx 0.3$, the average flow per unit length in the channel is approximately 10^{-2}, which is 10^8 times larger than that in the porous medium, 10^{-10}. More precisely, the ratio of average Stokes to Darcy flow is

$$\frac{\bar{u}_s}{\bar{u}_d} = \frac{\dfrac{lK^{1/2}}{2\mu\alpha} + \dfrac{l^2}{12\mu}}{\dfrac{K}{\mu}} = \frac{l}{2\alpha K^{1/2}} + \frac{l^2}{12K} \approx \frac{l^2}{12K} \approx 10^8. \tag{3.22}$$

We also obtain that the velocity on the interface, 10^{-6}, is approximately 10^4 times smaller than the flux in the channel. This information about the order of magnitude of the fluxes and the tangential velocity on the interface will be used in the definition of the prolongation operator.

Definition of the prolongation operators.

We use the notation that we introduced when we defined the coarsening strategy in Subsection 3.3.1. For each $k = M, M-1, ..., 0$, let V_x^k, V_y^k, and V_p^k denote the set of real valued functions defined on grids G_x^k, G_y^k, and G_p^k, respectively, and let $V^k = V_v^k \times V_p^k$, where $V_v^k = V_x^k \times V_y^k$. This notation is not completely rigorous since V_x^k, V_y^k and V_p^k are spaces of functions defined on different subgrids of G^k and the expression $(u_x, u_y, p)(t)$ for $(u_x, u_y, p) \in V^k$ and $t \in G^k$ would not make sense for some components. Nevertheless, for a given grid point $t \in G^k$, we usually write $u_x(t)$, $u_y(t)$ or $p(t)$, depending on the subgrid of G^k that t belongs to. For some purposes, we can identify V^k with $\mathbb{R}^{n_k+m_k}$, where n_k and m_k are the respective numbers of degrees of freedom for velocity and pressure for level k.

From now on, to simplify the notation we denote the prolongation operator P_{k-1}^k by P^k; thus, $P^k : V^{k-1} \to V^k$. We will define P^k in such a way that

$$P^k(u,p) = (P_v^k u, P_p^k p) \quad \text{for} \quad (u,p) = (u_x, u_y, p) \in V^{k-1}, \tag{3.23}$$

where $P_v^k : V_v^{k-1} \to V_v^k$ and $P_p^k : V_p^{k-1} \to V_p^k$. In matrix notation, P^k will be

$$P^k = \begin{bmatrix} P_v^k & 0 \\ 0 & P_p^k \end{bmatrix}. \tag{3.24}$$

Thus, our prolongation does not mix velocities and pressures.

We need to distinguish cases $k = M$ and $k < M$.

Case $k = M$.

Let $k = M$ and recall that $G_p^M = G_p^{M-1}$. We set P_p^M to be the identity operator on V_p^M.

Now let $u \in V_v^{M-1}$, and let $P_v^M u = w = (w_x, w_y) \in V_v^M$ be defined as follows. If $t \in G_x^M \setminus G_y^M$ (t is not a corner point), then we set $w_x(t) = u_x(t)$. Similarly, if $t \in G_y^M \setminus G_x^M$, then we set $w_y(t) = u_y(t)$. If $t \in G_x^M \cap G_y^M$ (t is a corner point) then we have two subcases (see Figure 3.7).

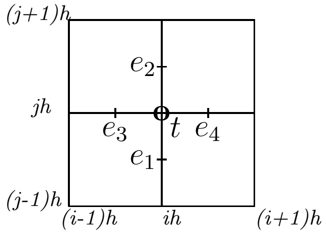

Figure 3.7: *Prolongation to the finest grid.*

In the first subcase, the 4 elements that share the corner $t = (ih, jh)$ are Stokes elements, i.e., they are contained in Ω_s. We do not expect to find jumps in the solution in this subcase, so we use linear interpolation. We recall that the order of the interpolation should be at least the order of the differential operator minus 1 [12]. Based on Figure 3.7, we define

$$w_x(t) = \frac{1}{2}(u_x(e_1) + u_x(e_2)),$$
$$w_y(t) = \frac{1}{2}(u_y(e_3) + u_y(e_4)),$$

where

$$e_1 = (ih, (j-1/2)h), \quad e_2 = (ih, (j+1/2)h),$$
$$e_3 = ((i-1/2)h, jh), \quad e_4 = ((i+1/2)h, jh).$$

In the second subcase, at least one of the four elements that has t as a corner is a Darcy element, i.e., is contained in Ω_d. We set $w_x(t) = w_y(t) = 0$. We make this choice because we observed in our simple model that the tangential velocity on the Darcy-Stokes interface is approximately 10^4 times smaller than the flux per unit length on the Stokes domain. Based on this argument, if, say, the top 2 elements were Stokes, we could have also set $w_x(t) = 10^{-4}u_x(e_2)$. However, in practice we saw very little difference between this and simply taking $w_x(t) = 0$.

Case $k < M$.

We now consider the case $k < M$. To prolongate the pressure, if $q \in V_p^{k-1}$, we define (see Figure 3.8)

$$P_p^k q(c_i) = q(C), \quad i = 1, 2, 3, 4, \tag{3.25}$$

where $c_i \in \{((i \pm 1/2)h_k, (j \pm 1/2)h_k)\}$ and $C = (ih_k, jh_k)$. The mapping P_p^k is clearly injective.

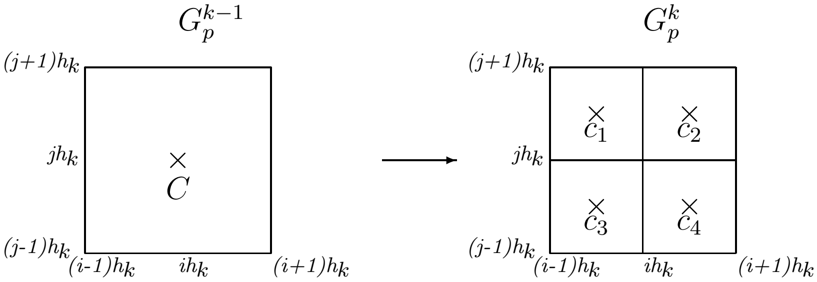

Figure 3.8: *Pressure prolongation from* G_p^{k-1} *to* G_p^k, $k < M$. *The pressure in each of the 4 finer cells is set equal to the pressure in the coarser-grid cell.*

For the velocity, as we mentioned above, we need to pay attention to the order of magnitude of the flux in the different subdomains. To this end, we label the edges on each grid according to the magnitude of the flux that we expect to observe.

On the finest grid G^M, if an edge is shared by at least one Darcy element (i.e., an element contained in Ω_d), then we expect the flow through this edge to be relatively small. We say that this is a D-edge. On the other hand, if an edge is shared by two Stokes elements (i.e., elements contained in Ω_s), then according to the model case analyzed at the beginning of this section, we expect the flux through this edge to be relatively large. It can be the case however, that the two Stokes elements are totally surrounded by Darcy elements (disconnected vugs) and then the flux should be comparable to that in the Darcy subdomain. So we first label every edge that has two adjacent Stokes elements as an S-edge. Then we run a few smoothing iterations on the finest-grid, which will be enough for us to get an idea of the order of magnitude of the flux through every edge. If after a few smoothing iterations, the flux through an S-edge is “small” (less than, say, 10^{-1} times the expected channel flow, which is 10^{-3} in our simple model case), then we relabel it as an S-d edge.

It is usually an edge shared by two Stokes elements that are "disconnected" from the rest of the Stokes subdomain Ω_s.

On coarser grids G^k ($k < M-1$), if an edge contains at least one finest-grid edge of type S, then we label it as an edge of type S. If an edge is not of type S and it contains at least one finest grid edge of type S-d, then we say that it is an S-d edge. Finally, an edge on a coarser grid which consists only of finest-grid D-edges will be a D-edge.

Let $u = (u_x, u_y) \in V_v^{k-1}$ and let $P_v^k u = w = (w_x, w_y)$. According to Figure 3.9, u is defined on the coarser-grid edges $\mathbf{e_1}$, $\mathbf{e_2}$, $\mathbf{e_3}$, and $\mathbf{e_4}$, and we should define w on the finer-grid edges $\{e_{i\pm}\}_{i=1,\dots,6}$.

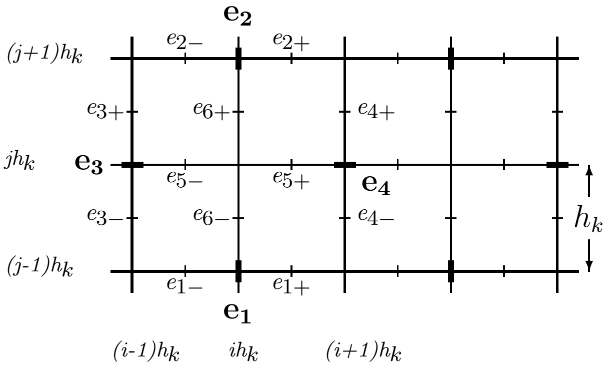

Figure 3.9: *Velocity prolongation for* $k < M$. *If* $w = P_v^k u$, *then* u *is defined on* $\mathbf{e_1}$, $\mathbf{e_2}$, $\mathbf{e_3}$, *and* $\mathbf{e_4}$, *and* w *is defined on* $\{e_{i\pm}\}_{i=1,\dots,6}$.

We first define w_x and w_y on the coarse grid boundaries, i.e., at $e_{1\pm} = ((i \pm 1/2)h_k, (j-1)h_k)$, $e_{2\pm} = ((i \pm 1/2)h_k, (j+1)h_k)$, $e_{3\pm} = ((i-1)h_k, (j \pm 1/2)h_k)$, and $e_{4\pm} = ((i+1)h_k, (j \pm 1/2)h_k)$, and then we define them in the interior at $e_{5\pm} = ((i \pm 1/2)h_k, jh_k)$ and $e_{6\pm} = (ih_k, (j \pm 1/2)h_k)$. If we assume that u and w approximately describe average fluxes per unit length, then

$$2hu_x(\mathbf{e_4}) \approx h(w_x(e_{4+}) + w_x(e_{4-})).$$

Suppose that the orders of magnitude of $w_x(e_{4+})$ and $w_x(e_{4-})$ are such that the ratio $\dfrac{w_x(e_{4+})}{w_x(e_{4-})} \approx f_4$, where $f_4 > 0$ is some factor to be discussed below. Then,

$$2hu_x(\mathbf{e_4}) \approx hw_x(e_{4-})(1+f_4) \approx hw_x(e_{4+})(1+f_4^{-1}).$$

Hence, we define

$$w_x(e_{4+}) = \frac{2}{1+f_4^{-1}} u_x(\mathbf{e_4}), \tag{3.26a}$$

$$w_x(e_{4-}) = \frac{2}{1+f_4} u_x(\mathbf{e_4}). \tag{3.26b}$$

Note that (3.26) implies that P_v^k is injective. Since P_p^k is also injective, P^k itself is injective. The value for f_4 will depend on the relative orders of magnitude of the flows through edges e_{4+} and e_{4-}. If edges e_{4+} and e_{4-} are both of the same type (S, S-d or D), then we obviously choose $f_4 = 1$. If edge e_{4+} is S and edge e_{4-} is either D or S-d, then according to (3.22) we should set $f_4 = \dfrac{h_k^2}{12K}$. If edge e_{4+} is S-d and edge e_{4-} is D, then good practical results were observed by choosing $f_4 = 10$, although convergence is not particularly sensitive to the choice. We similarly define

$$w_x(e_{3\pm}) = \frac{2}{1+f_3^{\mp 1}} u_x(\mathbf{e_3}), \tag{3.27}$$

$$w_x(e_{1\pm}) = \frac{2}{1+f_1^{\mp 1}} u_x(\mathbf{e_1}), \tag{3.28}$$

$$w_x(e_{2\pm}) = \frac{2}{1+f_2^{\mp 1}} u_x(\mathbf{e_2}). \tag{3.29}$$

Note that these definitions are edge-based, and so are well defined over the coarse grid boundaries.

Now to define $w_x(e_{6\pm})$ and $w_y(e_{5\pm})$ within the coarse grid cell (see Figure 3.9). We again assume that u and w approximately represent average fluxes per unit length. Let $\mathbf{e_6}$ denote the union of edges e_{6-} and e_{6+} and let $\mathbf{e_5}$ denote the union of edges e_{5-} and e_{5+}. If there are no sources inside the element, then an approximation of the total flux through $\mathbf{e_6}$ is given by the average of the fluxes that *go into* the element through edges $\mathbf{e_3}, e_{2-}$ and e_{1-}, and *out of* this element through edges e_{1+}, e_{2+}, and $\mathbf{e_4}$. Let w_6 denote the flux per unit length through $\mathbf{e_6}$, so

$$w_6 = \frac{1}{4}(2u_x(\mathbf{e_3}) + w_y(e_{1-}) - w_y(e_{2-}) + 2u_x(\mathbf{e_4}) + w_y(e_{2+}) - w_y(e_{1+})). \tag{3.30}$$

Using the same argument we used for $w_x(e_{4-})$ and $w_x(e_{4+})$, we define

$$\begin{aligned} w_x(e_{6+}) &= \frac{2}{1 + f_6^{-1}} w_6, \\ w_x(e_{6-}) &= \frac{2}{1 + f_6} w_6, \end{aligned}$$

where the value chosen for f_6 depends on the labels for edges e_{6+} and e_{6-}. Similarly, we define

$$w_y(e_{5\pm}) = \frac{2}{1 + f_5^{\mp 1}} w_5, \tag{3.32}$$

where

$$w_5 = \frac{1}{4}(2u_y(\mathbf{e_1}) + w_x(e_{3-}) - w_x(e_{4-}) + 2u_y(\mathbf{e}_2) - w_x(e_{3+}) + w_x(e_{4+})). \tag{3.33}$$

In summary, our prolongation operator is designed to prolongate fluxes in a physically appropriate way. As we noted, the difficulty is that vuggy media tend to contain Stokes channels with high flow rates. Our prolongation tries to recognize this fact. Initial smoothing identifies the channels. High fluxes in Stokes channels across coarse edges are prolongated in such a way that they are biased to the side containing the Stokes elements, and away from Darcy elements. This preserves the channeling structure throughout the multigrid procedure and improves convergence.

3.4 Well posedness

In this section, we prove that the coarse-grid operators L_k given by (3.6) are such that the corresponding linear systems are well posed. To that end, we recall a classical existence and uniqueness result for saddle point systems [13, 14]. We restrict ourselves to the finite dimensional case.

Lemma 3.4.1. *Let* E^n *and* E^m *be Hilbert spaces with dimension* n *and* m *respectively,* $n \geq m$*, and let* $a : E^n \times E^n \to \mathbb{R}$ *and* $b : E^n \times E^m \to \mathbb{R}$ *be bilinear forms. Assume that*

$$\sup_{w \in E^n} \frac{a(v,w)}{\|w\|} \geq \alpha \|v\| \quad \text{for all } v \in E^n, \tag{3.34a}$$

$$\sup_{v \in E^n} a(v,w) > 0 \qquad \text{for all } w \in E^n, \tag{3.34b}$$

$$\sup_{v \in E^n} \frac{b(v,q)}{\|v\|} \geq \beta \|q\|, \quad \text{for all } q \in E^m, \tag{3.34c}$$

where α *and* β *are positive constants. Then, for every* $(f,g) \in E^n \times E^m$*, there is a unique pair* $(u,p) \in E^n \times E^m$ *such that*

$$a(u,v) + b(v,p) = (f,v) \quad \text{for all } v \in E^n,$$

$$b(u,q) = (g,q) \quad \text{for all } q \in E^m.$$

Remark 3.4.1. *Condition* (3.34c) *is the so-called inf-sup condition. In the finite-dimensional case, it can be expressed in a simpler way. Let* $\mathcal{B} : E^m \to E^n$ *be given by*

$$(\mathcal{B}q, v) = b(v,q) \quad \text{for all } vinE^n,$$

where $(\cdot,\cdot)$ *denotes the inner product in* E^n*. Then condition* (3.34c) *is equivalent to* $Rank(\mathcal{B}) = m$*. To see this, we observe that* (3.34*c*) *is equivalent to*

$$\|\mathcal{B}q\| \geq \beta \|q\|. \tag{3.35}$$

Lemma 3.4.2. *For each* $k = M, M-1, ..., 0$*, let* L_k *be the discrete operator given by* (3.6) *when* $k < M$ *and by the matrix of system* (3.1) *when* $k = M$*. Then* L_k *has the form*

$$L_k = \begin{bmatrix} A^k & B^k \\ (B^k)^t & 0 \end{bmatrix}, \tag{3.36}$$

where A^k *is symmetric, positive definite and*

$$A^k = (P_v^{k+1})^t A^{k+1} P_v^{k+1}, \tag{3.37a}$$

$$B^k = (P_v^{k+1})^t B^{k+1} P_p^{k+1}. \tag{3.37b}$$

Proof. Successively from (3.6) and (3.24), for $k = M-1, ..., 0$,

$$\begin{aligned} L_k &= (P^{k+1})^t L_{k+1} P^{k+1} \\ &= \begin{bmatrix} (P_v^{k+1})^t & 0 \\ 0 & (P_p^{k+1})^t \end{bmatrix} \begin{bmatrix} A^{k+1} & B^{k+1} \\ (B^{k+1})^t & 0 \end{bmatrix} \begin{bmatrix} P_v^{k+1} & 0 \\ 0 & P_p^{k+1} \end{bmatrix} = \begin{bmatrix} A^k & B^k \\ (B^k)^t & 0 \end{bmatrix}, \end{aligned}$$

as claimed. Since A is positive definite and P_v^k is injective, A^k is also positive definite for each $k = M-1, .., 0$. □

We now state our main result.

Theorem 3.4.3. *Assume the hypotheses of Lemma* 3.4.2*, and let* $A = A^M$ *be of size* $n \times n$ *and let* $B = B^M$ *be of size* $n \times m$*, with* $n \geq m$*. Then* B^k *has full rank and the system*

$$L_k x = c \tag{3.38}$$

has a unique solution $x \in V^k$ *for any* $c \in V^k$*, for* $k = M, M-1, ..., 0$*.*

Proof. Since A^k is symmetric, positive definite by Lemma 3.4.2, the solvability result (3.38) follows from Lemma 3.4.1 and Remark 3.4.1 once we establish that B^k has full rank.

Rank is a property independent of basis. We use the basis described in Subsection 2.2.2. On the finest grid G^M, let $\mathbf{v}_e^i$ be the edge (or face) velocity basis function which has average normal flux equal to 1 at edge e_i of the grid G^M and is or has normal average flux 0 at any other point of G^M, and let $\mathbf{v}_c^\ell$ be the corner velocity basis function which is 1 at corner c_ℓ and is or has average flux 0 at any other point of G^M. Let $w_j : \Omega \to \mathbb{R}$ equal 1 on element E_j and 0 elsewhere. Now the elements of matrix B have the form

$$\begin{aligned} B_{ij} &= \int_\Omega \nabla \cdot \mathbf{v}_e^i \, w_j \, dx = \int_{e_i \cap \partial E_j} \mathbf{v}_e^i \cdot \nu \, dx \\ &= \begin{cases} h & \text{if cell } E_j \text{ is located to the left of or below } e_i, \\ -h & \text{if cell } E_j \text{ is located to the right of or above } e_i, \\ 0 & \text{otherwise,} \end{cases} \end{aligned} \tag{3.39}$$

or

$$B_{\ell j} = \int_\Omega \nabla \cdot \mathbf{v}_c^\ell \, w_j \, dx = \int_{\partial E_j} \mathbf{v}_e^i \cdot \nu \, dx = 0. \tag{3.40}$$

That is, B^t is a matrix of divergence type, in the sense that it is constructed as (see Figure 3.10 for notation)

$$B^t u(c) = h(u(e_2) - u(e_1) + u(e_4) - u(e_3)). \tag{3.41}$$

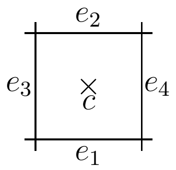

Figure 3.10: *A typical cell of the grid G^M. We have that B^t is the discrete divergence operator on G_v^M.*

Now

$$B_{ij}^{M-1} = \sum_{m,k} (P_v^M)_{mi} B_{mk} (P_p^M)_{kj} = \sum_k B_{ik} (P_p^M)_{kj} = B_{ij},$$

since when index m corresponds to a corner, $B_{mk} = 0$, and when m corresponding to an edge, $(P_v^M)_{mi} = \delta_{mi}$. That is, B^{M-1} is obtained from B by removing the identically vanishing rows (3.40) that correspond to corner points of the finest grid. Moreover, (3.39) also holds for B^{M-1}, and $(B^{M-1})^t : V_v^{M-1} \to V_p^{M-1}$ is again a discrete divergence operator (see Figure 3.10)

$$(B^{M-1})^t u(c) = h(u(e_2) - u(e_1) + u(e_4) - u(e_3)).$$

We now show that $(B^k)^t : V_v^k \to V_p^k$ is the discrete divergence operator for $k = M-2, ..., 0$. Let $u \in V_v^{M-2}$. Then by (3.37), (3.25), (3.41) and (3.26) (see Figure 3.11 for notation)

$$\begin{aligned}
(B^{M-2})^t u(C) &= (P_p^{M-1})^t (B^{M-1})^t P_v^{M-1} u(C) \\
&= \sum_{i=1}^{4} (B^{M-1})^t P_v^{M-1} u(c_i) \\
&= h[P_v^{M-1}u(e_{2-}) + P_v^{M-1}u(e_{2+}) - P_v^{M-1}u(e_{1-}) - P_v^{M-1}u(e_{1+}) \\
&\quad - P_v^{M-1}u(e_{3-}) - P_v^{M-1}u(e_{3+}) + P_v^{M-1}u(e_{4-}) + P_v^{M-1}u(e_{4+})] \\
&= 2h(u(\mathbf{e_2}) - u(\mathbf{e_1}) - u(\mathbf{e_3}) + u(\mathbf{e_4})).
\end{aligned} \tag{3.42}$$

We have used that the terms corresponding to internal edges in Figure 3.11 cancel out because the contributions from the two elements that share each edge have opposite signs. Repeating the argument inductively we obtain that the claim is true for every k.

It is well known that such a discrete divergence matrix $(B^k)^t$, $k = M, M-1, ..., 0$, maps onto and therefore has full rank. One argument comes from looking at the finite element discretization of the mixed formulation of the following auxiliary elliptic problem, using an appropriate finite element

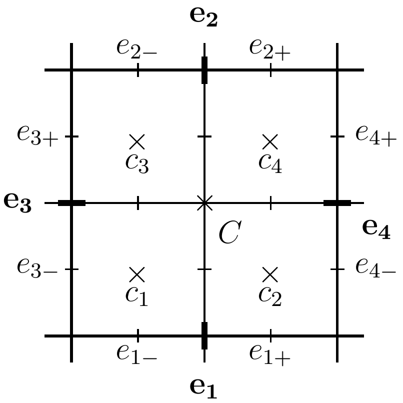

Figure 3.11: *Grid G^{M-1} with coarser grid G^{M-2} in bold.*

space (for example, lowest order Raviart-Thomas spaces [24, 14]):

$$\begin{aligned} -\Delta f &= 0 \quad \text{in } \Omega, \\ f &= f_0 \quad \text{on } \partial\Omega \setminus C, \\ \nabla f \cdot \nu &= 0 \quad \text{on } C, \end{aligned}$$

where f_0 is some known function defined on $\partial\Omega \setminus C$ and ν is the outer unit normal to $\partial\Omega$. The full rank property of the discrete divergence operator is a consequence of the unique solvability of this discretized auxiliary problem.

The proof of the theorem is now complete. □

Remark 3.4.2. *In general, it is not possible to construct A^k more simply than as given recursively in* (3.37)*. However, we have shown that, in the natural basis of Subsection* 2.2.2*, each $(B^k)^t$ is easily constructed as a discrete divergence, and, conversely, each B^k is a (negative) discrete gradient. We used this observation to write a simpler and more efficient computer code to implement the multigrid procedure.*

Remark 3.4.3. *If $C = \partial\Omega$, it can be seen from* (2.14) *that the pressure p is* *determined only up to a constant; that is, p belongs to* $W = L^2(\Omega)/\mathbb{R}$. *The appropriate space* V_p^k *for the discretized pressure is the set of grid functions defined on* G_p^k *which have average* 0. *For* $k = M-1, ..., 0$, *the operators* $(B^k)^t$ *are again discrete divergence operators and continue to have full rank, this time equal to* $m_k - 1 = dim(V_p^k)$, *where* m_k *is the number of elements for level* k. *The justification of this fact comes from the same type of argument we used above for the other boundary conditions, but now the auxiliary problem reads*

$$-\Delta f = 0 \quad in\ \Omega,$$

$$\nabla f \cdot \mu = 0 \quad on\ \partial\Omega.$$

The rest of the statements of Lemma 3.4.2 *and Theorem* 3.4.3 *remain true in this case.*

Chapter 4

Observed Convergence of the Multigrid Method

We illustrate the performance of our method by computing the flow for the two dimensional Darcy-Stokes system shown in Figure 4.1. Pressure Dirichlet boundary conditions are used, where $p = 1$ on the bottom and left boundary faces, and $p = 0$ on the other two faces. Obviously, matrix A in (3.1) depends on the spatial arrangement of the Darcy and Stokes subdomains. The more intertwined they are, the more irregular the coefficients of A will be.

```
0 0 — — 0 0 0 — 0 0 — — 0 0 0 —
0 0 — — — 0 0 0 0 0 — — — 0 0 0
0 — — 0 — — — 0 0 — — 0 — — — 0
— — 0 0 0 0 — — — — 0 0 0 0 — —
— — 0 0 0 — — — — — 0 0 0 — — —
0 — — 0 — — 0 0 0 — — 0 — — 0 0
0 0 — — — 0 0 0 0 0 — — — 0 0 0
0 0 0 — — 0 — — 0 0 0 — — 0 — —
0 0 — — 0 0 0 — 0 0 — — 0 0 0 —
0 0 — — — 0 0 0 0 0 — — — 0 0 0
0 — — 0 — — — 0 0 — — 0 — — — 0
— — 0 0 0 0 — — — — 0 0 0 0 — —
— — 0 0 0 — — — — — 0 0 0 — — —
0 — — 0 — — 0 0 0 — — 0 — — 0 0
0 0 — — — 0 0 0 0 0 — — — 0 0 0
0 0 0 — — 0 — — 0 0 0 — — 0 — —
```

Figure 4.1: *A domain representing a porous medium with vugs. Each* 0 *represents a Darcy element and each dash a Stokes element.*

In this Chapter, we use a relatively poor smoother compared to that presented in Subsection 3.3.3. We simply use an unmodified Uzawa smoother and take $C = diag(B^t \widehat{A}^{-1} B)$. This emphasizes the multigrid procedure itself, and allows us to assess its value in solving (3.1) as opposed to the effectiveness of the smoother.

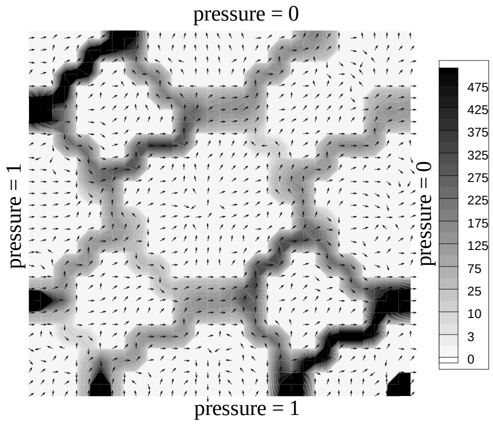

Figure 4.2: *Fluid flow for the system of Figure 4.1 obtained with our multigrid algorithm. The arrows indicate the direction of the flow. The gray tones indicate speed or average flux per unit length.*

Figure 4.2 shows the velocity field that we obtained. The stopping criterion was that the scaled difference between two consecutive smoothing iterations on the finest grid be smaller than 10^{-12}. Notice the large jumps in the flux per unit length between different regions. The flux in the porous matrix as well as that in the disconnected vugs has values between 10^{-7} and 10^{-5}, while the flux in the connected vugs is in the range of several hundreds. As we mentioned in Section 3.4, taking into account the very different orders of magnitude of the Darcy and Stokes flows is crucial in order to obtain a convergent multigrid algorithm. In fact, if we run our multigrid code with different values for parameter f (see (3.26)), we observe that non-physical values make the algorithm diverge.

```
0 0 — — 0 0 0 0 0 0 — — 0 0 0 0
0 0 — — — 0 0 0 0 0 — — — 0 0 0
0 — — 0 — — — 0 0 — — 0 — — — 0
— — 0 0 0 0 — — — — 0 0 0 0 — —
— — 0 0 0 — — — — — 0 0 0 — — —
0 — — 0 — — 0 0 0 — — 0 — — 0 0
0 0 — — — 0 0 0 0 0 — — — 0 0 0
0 0 0 — — 0 0 0 0 0 0 — — 0 0 0
0 0 — — 0 0 0 0 0 0 — — 0 0 0 0
0 0 — — — 0 0 0 0 0 — — — 0 0 0
0 — — 0 — — — 0 0 — — 0 — — — 0
— — 0 0 0 0 — — — — 0 0 0 0 — —
— — 0 0 0 — — — — — 0 0 0 — — —
0 — — 0 — — 0 0 0 — — 0 — — 0 0
0 0 — — — 0 0 0 0 0 — — — 0 0 0
0 0 0 — — 0 0 0 0 0 0 — — 0 0 0
```

Figure 4.3: *A Darcy-Stokes system obtained from that of Figure 4.1 by removing disconnected vugs.*

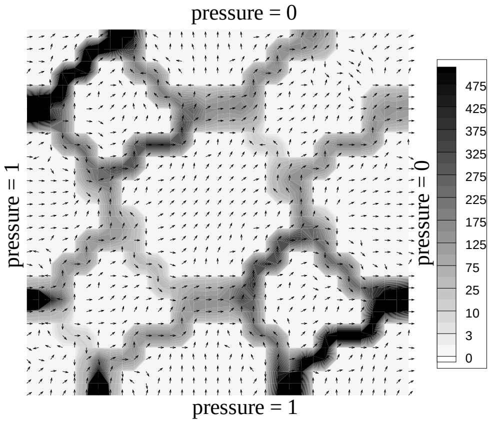

Figure 4.4: *Fluid flow for the system of Figure 4.3 obtained with our multigrid algorithm.*

The measured convergence factor of our method, as we will see, turns out to be independent of the size of the system, or equivalently, independent of the mesh size h, as far as the system under consideration had no disconnected vugs, i.e., the system has no vugs totally surrounded by Darcy elements. One example is the system shown in Figure 4.3, which has been obtained from that of Figure 4.1 by removing the disconnected vugs. The corresponding flow field is shown in Figure 4.4.

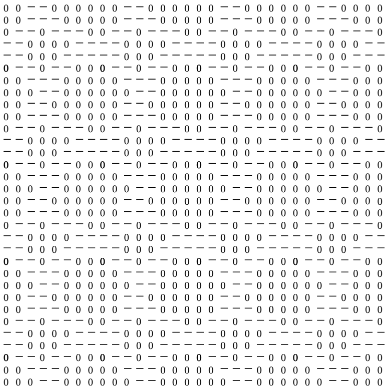

Figure 4.5: *A Darcy-Stokes system obtained by combining 4 replicas of the system shown in Figure 4.3 and rescaling.*

In most cases where a multigrid algorithm is investigated, the continuous differential problem to be solved is independent of the discretization of the domain. For example, we might want to solve Laplace's equation with appropriate boundary conditions. In order to analyze the convergence factor, the method that is being studied is tested for a set of domain discretizations. In our case, things are different because (2.14)–(2.15) depends on the spatial arrangement of the Darcy and Stokes subdomains. Therefore, to study the convergence factor, we need to consider decreasingly smaller values of h for the *same type of system*. To achieve this effect, we combine 4 replicas of systems with mesh size h like the one shown in Figure 4.3, and then rescale it to obtain a system with mesh size $h/2$ (see Figures 4.5–4.6). We then repeat this process to obtain a family of systems with the same pattern of Darcy-Stokes intertwining and progressively smaller mesh sizes. Obviously, the measured convergence factor will depend on the specific pattern of Darcy-Stokes intertwining under consideration.

The measured convergence factor ρ^n and averaged convergence factor

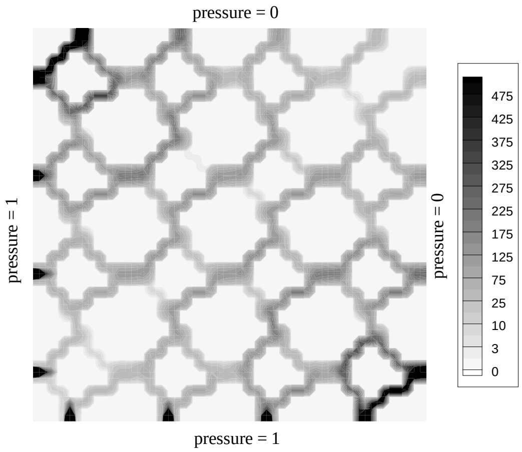

Figure 4.6: *Fluid flow for the system of Figure 4.5. The arrows indicating the direction of the flow have been removed.*

	$h = 1/16$	$h = 1/32$	$h = 1/64$	$h = 1/128$
ρ^n	0.03780	0.04591	0.03908	0.03862
$\tilde{\rho}^n$	0.03901	0.04569	0.03379	0.03662

Table 4.1: *Measured convergence factors and averaged convergence factors for different "discretizations" of the system of Figure 4.3.*

$\tilde{\rho}^n$ were computed using the formulas

$$\rho^n = \frac{\|r^n\|_2}{\|r^{n-1}\|_2} \quad \text{and} \quad \tilde{\rho}^n = (\rho^2 \rho^3 \cdots \rho^n)^{1/(n-1)},$$

where r^n is the residual after the nth multigrid iteration and $\|\cdot\|_2$ denotes the discrete l_2 norm. The results shown in Table 4.1 correspond to the systems of Figure 4.3 ($h = 1/16$), Figure 4.5 ($h = 1/32$) and two finer "discretizations" ($h = 1/64$ and $h = 1/128$). The coarsest grid was 8×8 elements. The results show a very good multigrid convergence factor: the error is reduced by a factor of about 0.04 each V-cycle.

The measured convergence factor for the system of Figure 4.5, but with disconnected vugs (i.e., 4 copies of Figure 4.1), was only 0.59, and, in general, the factor was *not* independent of the "mesh size." Moreover, for some systems with disconnected vugs, the convergence rate was very slow unless the coarsest grid was sufficiently fine. This is a well known fact about multigrid methods for a saddle point system such as (3.1), which has both positive and negative eigenvalues. They require a coarsest grid fine enough for some components of the error to be eliminated [12].

Chapter 5

Numerical Studies of Transport Properties of Vuggy Media

In this chapter, we use model (2.1)–(2.10) and its variational formulation (2.14)–(2.15) to study transport and flow properties of vuggy media by simulations. We use the multigrid method described in Chapter 3 to solve the discretized system (3.1). As we will see in the examples, all the simulations are done in three dimensional space.

Transport properties of vuggy porous media is a topic of great interest for the engineering community. Besides its practical implications (for example, in the study of contaminant transport or in petroleum production), tracer experiments might provide information about the heterogeneities of vuggy rocks. In [32], several tracer experiments were performed on vuggy rocks of carbonate type. Based on the results of those experiments, hypotheses were presented about the vug connection pattern in the rock. Our main goal in this chapter is to add some insight to this analysis by doing numerical simulations. Although we use the term simulation, we admit that our cases are rather simple, toy patterns of a vuggy porous medium. Including all the complexity of a real vuggy rock would imply working on a problem of such size that only a parallel code would be able to handle it. We plan to do such a study in the future. However, the simple cases that we present here allow us to formulate new transport mechanisms that explain the experimental observations described in [32].

5.1 A tracer experiment

The Pipe Creek Reef is a well known Cretaceous (Albian) rudist buildup in the Glen Rose Formation in Central Texas [23]. The outcrop is exhumed by Red Bluff and Pipe Creek, but is dry for much of the year. It is one of the best exposed rudist reefs in the world [22] (see Figure 5.1). Several different types of rudist fossils are observed at this outcrop, but the most important reef-building varieties were the caprinids, which are the largest of the rudists at this location, had the thickest shell walls, lived in the highest wave-energy environments, and produced the most complicated large-scale pore networks (see Figure 5.2).

An approximately 36 cm high by 25 cm diameter sample was collected from the site, and imaged by a high-resolution X-ray CT scanner, showing its internal vug structure (see Fig. 5.3). A total of 240 slices were taken, each 1.5 mm thick and 28 cm by 28 cm with 512 by 512 pixels (i.e., about 0.55 mm square).

A tracer experiment was performed in this sample, and reported in [32]. First, a steady state flow of tap water is run through the Pipe Creek sample. In a second step, tap water flow is interrupted and salt water is injected. By using a system of valves and operating quickly, mixture between tap water and salt

Figure 5.1: *The Pipe Creek Reef.*

Figure 5.2: *Pipe Creek Reef vugs produced from rudist fossils.*

water is negligible at the site of injection, so that salt water injection can be modeled as a step function (tracer concentration jumps “instantaneously” from 0 to a finite value). In the third step, salt water injection is stopped and tap water is run again through the sample. Once again, this is performed in such a way that the tracer concentration of the injected fluid can be considered to drop

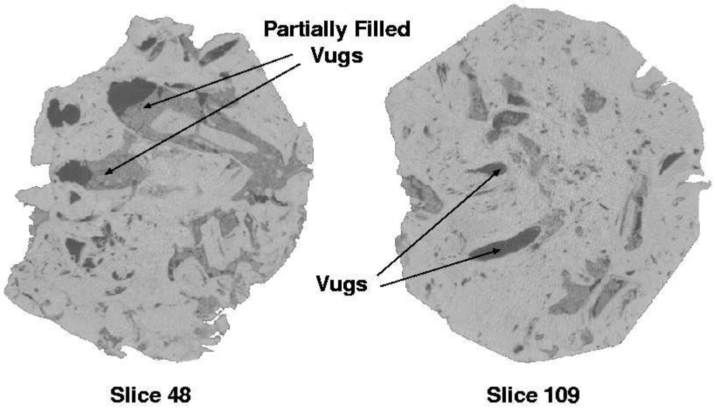

Figure 5.3: *Two CT scan cross-sections of the large sample from Pipe Creek Reef.*

as a step function "instantaneously" to zero. The setup of the experiment is such that the fluid flows through the rock by gravity. The tracer concentration of the effluent and the volume of fluid collected, is measured at different time intervals and a tracer concentration history is obtained.

A typical experimental plot is shown in Figure 5.4, showing the effluent tracer concentration versus time (actually, pore-volumes of collected fluid, which is proportional to time). There is an early breakthrough, so the tracer concentration rises quickly. It is interesting that it forms several high plateaus until it reaches its maximum. After some time, when the main injection ends, the curve drops quickly until it forms a rather unique feature, a single plateau. Finally, a long tail of decreasing tracer concentration in the effluent appears.

The author in [32] hypothesizes that the early breakthrough and initial concentration increase indicate the presence of a primary fast flow path. Moreover, other secondary fast paths give rise to the multiple plateaus on the ascending part of the plot. As we will see, our simulations support this idea.

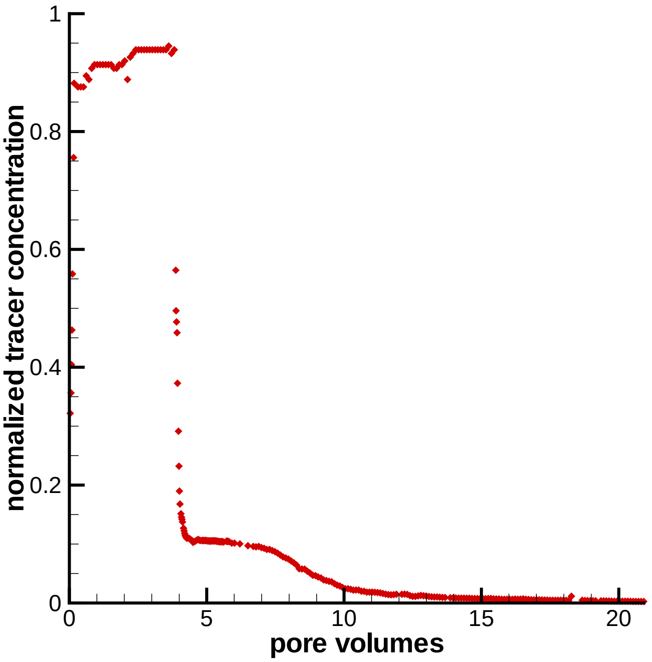

Figure 5.4: *A typical experimental plot of the normalized effluent tracer concentration as a function of the number of pore volumes collected. The pore volume of the sample, which is the maximum volume of fluid that can fill the rock pore space, was estimated from X-ray computed tomography data.*

To explain the single plateau that appears immediately after the rapid descent of the effluent concentration, it is argued that there are dead-end vugs in the rock that communicate with the flow paths. The tracer arrives in the dead-end vugs and is transported at a later time back to the main flow paths by a mechanism that could involve advection and/or diffusion. The tracer coming from the dead-end vugs would produce the late single plateau observed in the experimental plot. Based on our simulations, we propose an alternative mechanism for the single plateau. Basically, we propose that the single plateau is produced by branchings of the main flow paths. This gives raise not to dead-end vugs, but to relatively slower paths which yet remain very well interconnected to the main flow paths. According to our simulations, the dead-end vugs play only a very minor role in the experiment.

5.2 Computational simulations

In our simulations, we first computed a velocity field for the fluid flow, based on (2.1)–(2.10), using the multigrid method of Chapter 3 to solve the discretized system (3.1). We then used this flow to solve the transport problem, described below.

In all cases, except when specified otherwise, the simulations are performed using an $8 \times 8 \times 4$ cm^3 rectangular domain representing a vuggy porous medium. The discretization mesh size was $h = 0.5$ cm (i.e., a $16 \times 16 \times 8$ grid). We used mixed boundary conditions, in which given constant pressures on two opposite faces established a pressure gradient that drove the flow. On the other 4 faces, we assumed a zero normal flux condition. The given pressures were such that the magnitude of the force acting on a fluid element was roughly similar to that of gravity, as in the experiment. We set μ in (2.1)–(2.10) to be equal to water viscosity, permeability $K = 10$ md $\approx 9.8697 \times 10^{-11}$ cm^2, and the dimensionless Beavers-Joseph constant $\alpha = 1$. The force term f and the source g were both set equal to zero.

When our multigrid algorithm was used to solve (3.1), optimal results for the Uzawa smoothing procedure were obtained by choosing both parameters, a and b, in (3.11), equal to 0.6. We considered smoothing to be inefficient when the ratio of the residuals corresponding to two consecutive smoothing iterations was greater than 0.98. Every time this happened, we descended to the immediately coarser grid to find a solution of the residual equation. We used $M = 3$ multigrid levels, so the coarsest grid system corresponded to a partition of our domain into 4^3 elements (i.e., grids of size 16^3 with corners, 16^3 without corners, 8^3, and finally 4^3). The coarsest grid system was solved exactly by matrix factorization using the LAPACK software [1]. The multigrid algorithm stopping criterion was that the relative difference between the solutions obtained in two consecutive Uzawa iterations performed on the finest grid be smaller than the tolerance value 10^{-9}.

As we mentioned above, we used the computed velocity field $\mathbf{u}$ to solve the transport problem, which is the advection-diffusion/dispersion equation

$$\phi \frac{\partial c}{\partial t} + \nabla \cdot (c\mathbf{u} - \mathbf{D}\nabla c) = 0, \tag{5.1}$$

with boundary conditions

$$(\mathbf{u}c - \mathbf{D}\nabla c) \cdot \nu = c_B \mathbf{u} \cdot \nu, \quad \text{if } \mathbf{u} \cdot \nu < 0, \tag{5.2}$$

$$\mathbf{D}\nabla c \cdot \nu = 0, \qquad\qquad \text{if } \mathbf{u} \cdot \nu \geq 0, \tag{5.3}$$

where c denotes the tracer concentration, $\mathbf{u}$ is the velocity of the fluid, ϕ is the porosity of the rock, and $\mathbf{D}$ is the diffusion/dispersion tensor, given by

$$\mathbf{D}(\mathbf{u}) = \phi d_{\text{mol}} \mathbf{I} + |\mathbf{u}| \left\{ d_{\text{long}} \mathbf{E}(\mathbf{u}) + \mathbf{d}_{\text{trans}} (\mathbf{I} - \mathbf{E}(\mathbf{u})) \right\}, \tag{5.4}$$

where $\mathbf{I}$ is the identity tensor, $\mathbf{E}(\mathbf{v})$ is the tensor that projects onto the $\mathbf{v}$ direction, so the (i, j) component is

$$(\mathbf{E}(\mathbf{v}))_{i,j} = \frac{v_i v_j}{|\mathbf{v}|^2},$$

and d_{mol} is the molecular diffusion coefficient, and d_{long} and d_{trans} are the longitudinal and transverse dispersion coefficients respectively.

Boundary condition (5.2) is an inflow condition, where a normal advective flow is specified. The function c_B in our case is a square pulse, i.e.,

$$c_B(t) = \begin{cases} 1 & \text{for } 0 \leq t \leq t_0, \\ 0 & \text{for } t > t_0, \end{cases}$$

where t_0 is the pulse duration. In our simulations, the pulse duration $t_0 =$ 40 sec and we observed the effluent tracer concentration for 300 sec.

We used the following values for the parameters that appear in the transport equation (5.1), as given in the cgs unit system. In the Darcy region, $\phi = 0.08$, $d_{\text{long}} = 0.04$, and $d_{\text{trans}} = 0.008$. In the Stokes region, $\phi = 1$, $d_{\text{long}} = 0.00025$, and $d_{\text{trans}} = 5 \times 10^{-5}$. In both regions, $d_{\text{mol}} = 10^{-6}$.

For the numerical solution of (5.1), we use the code Parssim [3]. For this code, in each time step, concentration was first updated using the transport part of the equation by an explicit, second order Godunov method. In a few cases, we use a first order Godunov method, since the solutions are not very smooth. Using the concentration just obtained, we updated it again implicitly from the diffusion/dispersion part of the equation, using the cell-centered finite difference technique. A Jacobi preconditioned conjugate gradient method is used to solve the resulting linear system.

We report the "effluent tracer mass" history by extracting the following information for each time. For an injection of 1 g/cc, we report the total mass of tracer in the grid cells bounding the outflow face. This total is computed by summing over the 128 outflow cells. The quantity computed is the tracer concentration times the porosity (0.08 in the rock, and 1.0 in the vugs) times the cell volume (0.5^3 cc). This is not strictly the effluent, which should be velocity weighted and computed over the outflow face itself. However, this quantity qualitatively gives the shape of the true effluent curve and so is sufficient for determining the behavior of the system.

We now present the cases we examined in our simulations.

5.2.1 A simple channel configuration

The flow computed for a sample consisting of a simple vug channel in a porous matrix is shown in Figure 5.5. Although we do not depict the vug structure, it is clearly evident from the flow field. The velocity is nonzero in the entire domain, but it is highly concentrated in the vug channel. Our flow fields go from the back left face to the front right face.

The corresponding effluent tracer mass history is given in Figure 5.6. As mentioned above, we report the total mass on the out-flow face. This is not strictly comparable to the actual experiment, since the effluent would be velocity weighted. Nevertheless, as we can observe, the injected pulse of concentrated fluid is displaced by advection and minimally smoothed out by diffusion and dispersion on this very short time scale (300 sec). No plateaus are observed with this simple vug geometry. Thus, a single channel cannot account for the dynamics of tracer transport in the Pipe Creek sample.

A long tail is observed. This is due to diffusion/dispersion from the vug channel into the matrix rock in the cells at the outflow face. Recall that we do not velocity weight the effluent, so this tail is relatively large. It will also persist for a long time, since matrix flow is so slow.

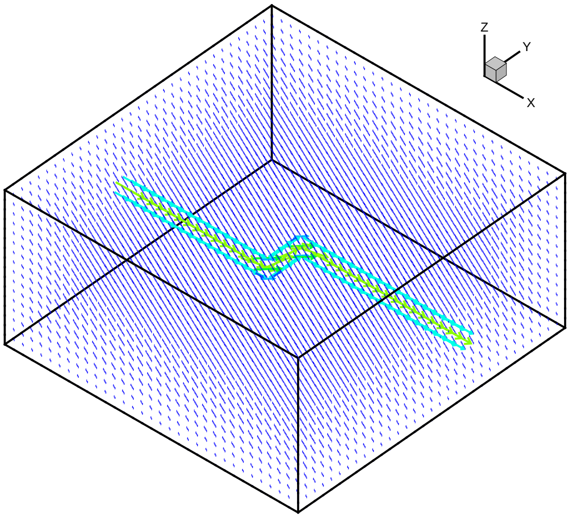

Figure 5.5: *Flow computed for a sample of porous rock with a simple channel.*

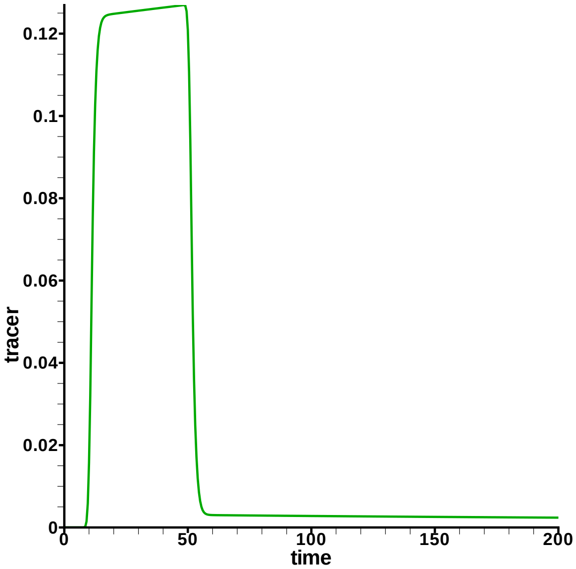

Figure 5.6: *Effluent mass history for the simple channel configuration. The corresponding flow is shown in Figure 5.5*

5.2.2 A bypass configuration

An important case is the one illustrated in Figure 5.7, which we call a bypass configuration. The effluent tracer mass history that was obtained is shown in

Figure 5.8. Because of the geometry of the vugs, there is a difference in the velocity of the flow in both branches (see the velocity scale in Figure 5.7). In this particular case, the velocity in the faster branch was approximately twice the velocity in the slower branch.

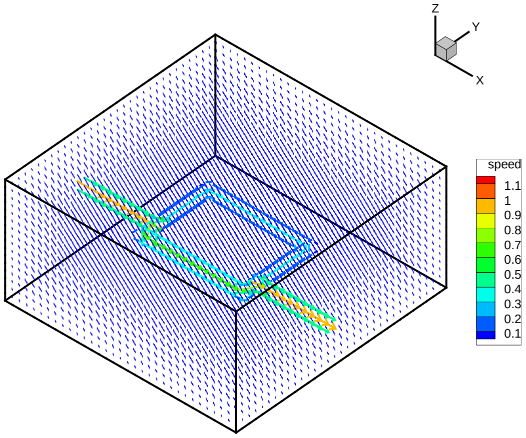

Figure 5.7: *Computed flow for a bypass configuration*

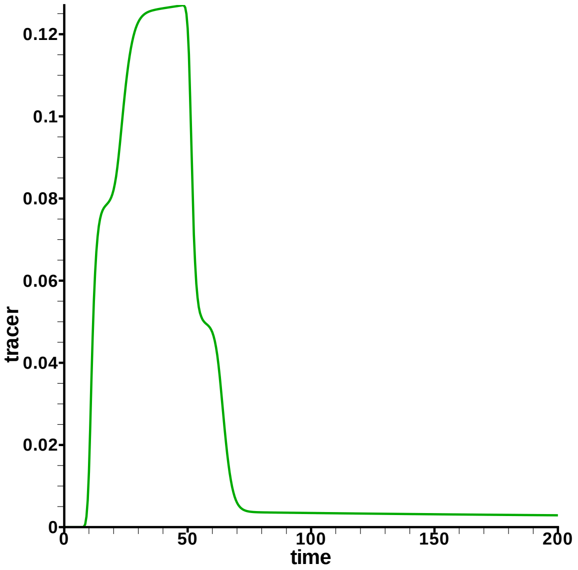

Figure 5.8: *Effluent mass history for the bypass configuration of Figure 5.7*

The pattern observed in Figure 5.8 suggests the following interpretation. The flow through the faster branch determines the early breakthrough in the tracer mass of the effluent. A short time after the mass has started to rise, a plateau is observed. Next, the slope increases again, due to the tracer that has reached the rock out-flow face coming from the slower flow path. The mass continues to rise until a maximum value is attained. At this point, the tracer that has traveled only through the faster path starts to decrease rapidly, a short time after injection has stopped. However, the effluent, being primarily the sum of the fluids from the two paths, still contains tracer from the slower path. When this happens, a small plateau is observed during the descending part of the mass curve. Finally, the tracer coming from the rock becomes progressively more diluted and a long tail is obtained, presumably due to diffusive and/or dispersive processes.

Roughly speaking, the pattern of Figure 5.8 can be thought of as the superposition of two curves without plateaus like the one of Figure 5.6 with different amplitudes and different timing. This is, of course, an oversimplification. In a bypass case, the faster and the slower flow paths are not independent, but interact with each other. The faster path receives a pulse of highly concentrated tracer fluid from the slower path at a delayed time, and this phenomenon gives rise to the plateaus in the effluent mass, even though there are no dead-end branches in the system.

At this point, it is reasonable to believe that we need a differential velocity between different flow paths to observe plateaus. This is confirmed by the simulation performed on a symmetric vug pattern. In Figure 5.9, the vug geometry and computed flow for a bypass case with symmetry is shown. The flow is identical in both flow paths, so, as expected, no plateaus are observed in the effluent tracer mass history (see Figure 5.10). We do, however, see some kind of mixing effect that is apparently not observed in the experiments.

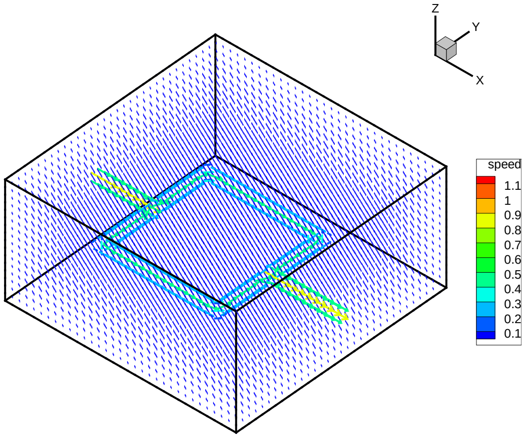

Figure 5.9: *Flow for a symmetric bypass configuration. Notice the symmetry in the magnitude of the flow in both branches*

There are infinitely many possibilities for bypass cases with the same effect as the one of Figure 5.7. Each particular geometry gives rise to a similar but unique mass history curve. The timing and the magnitude of the plateaus depend on the difference in velocity and total flux through each path and the distance that the tracer particles must travel through the slower path. Other bypass configurations are shown in Figure 5.11.

A special bypass case is the one where the slower path is a vug or channel much thinner than the main path. We consider the pattern of Figure 5.12. The wider vug has a cross section 2.5 mm × 5 cm, and the thin branch is 2.5 mm × 2.5 mm, so the thin vug cross section is 20 times smaller than that of the

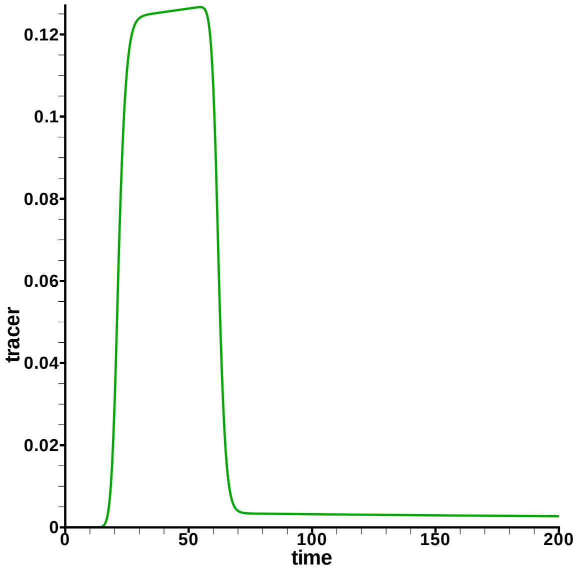

Figure 5.10: *Effluent tracer mass history for the symmetric bypass configuration of Figure 5.9. No plateau is observed*

main flow path. As we can observe in the tracer mass history of Figure 5.13, the plateau occurs quite late, after the descending part of the mass curve has almost come to an end. This late plateau is the result of a considerable delay in the flow through the thin vug compared to that in the main path, which generates a late small pulse of tracer into the effluent.

5.2.3 Multiple branches and multiple paths

In a sample of real rock, we find several independent flow paths, so we also studied in our simulations the presence of multiple branches and multiple paths. The geometry of the vugs and the computed flows are shown in Figure 5.14. Their respective tracer mass histories are shown in Figure 5.15. In the multiple branches case, the presence of the plateaus can be explained by a similar mechanism as that for a bypass case. In the case of multiple paths,

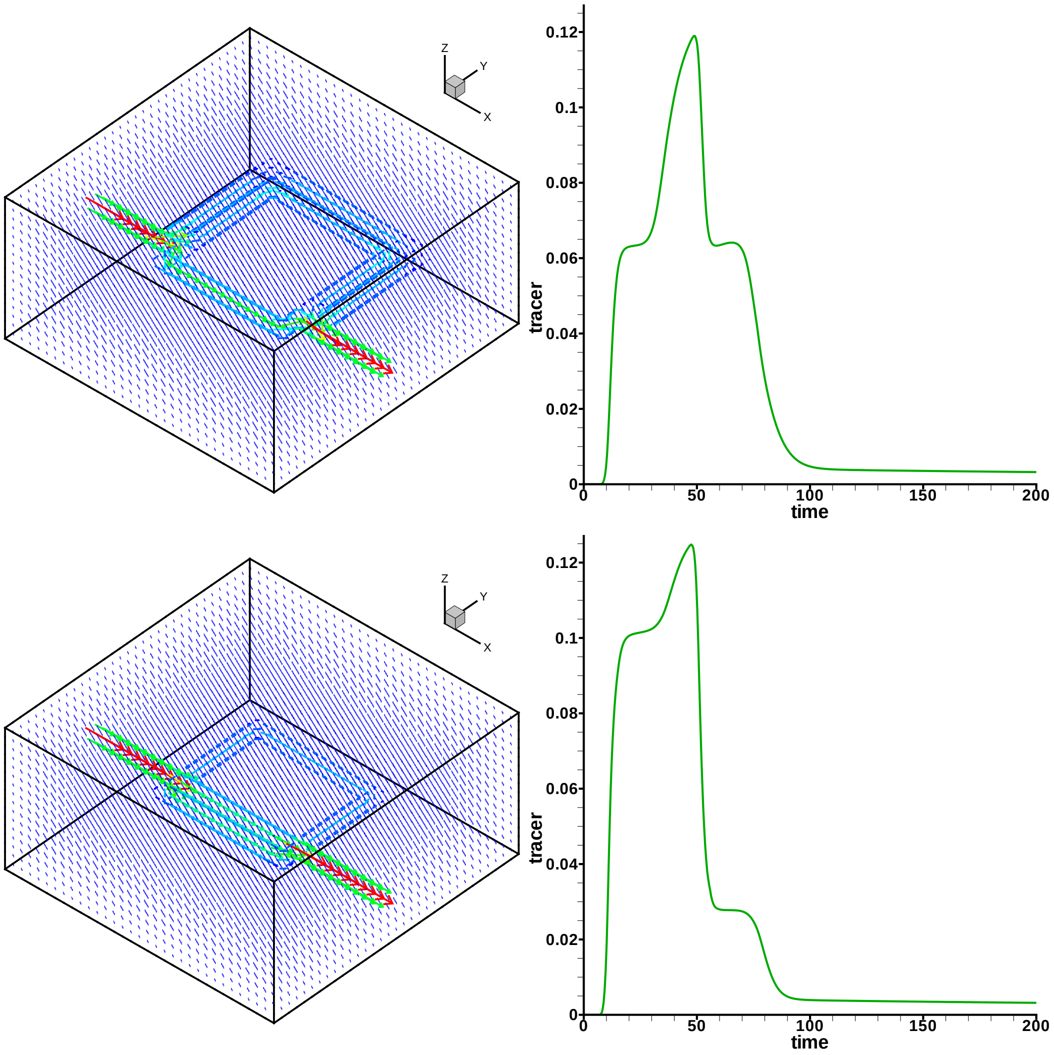

Figure 5.11: *Different bypass branches produce different tracer mass histories.*

the mechanism is even simpler, since the resulting tracer mass is essentially the average of those corresponding to each individual path, since matrix rock flow is so small. Because the paths have different travel times, we again obtain prominent plateaus in the effluent tracer mass history.

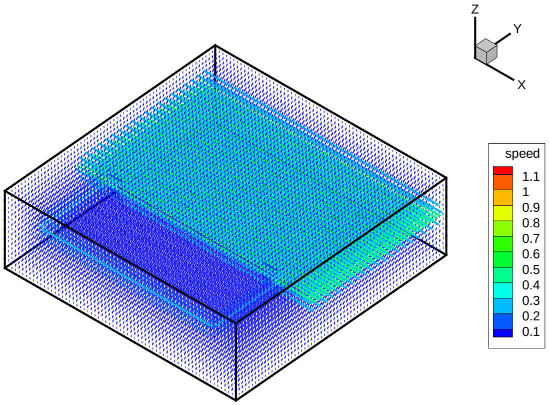

Figure 5.12: *Bypass case where a thin vug branches out from the main flow path.*

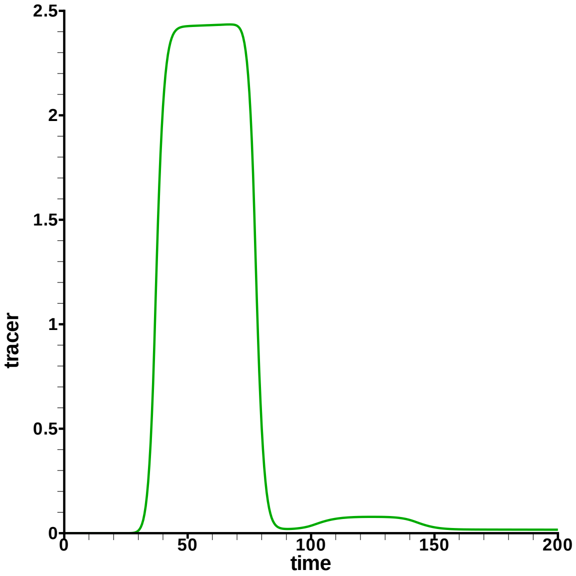

Figure 5.13: *Tracer mass history for the flow of Figure 5.12. A late single plateau is observed when a bypass branch contains a vug which is very thin compared to the main flow path.*

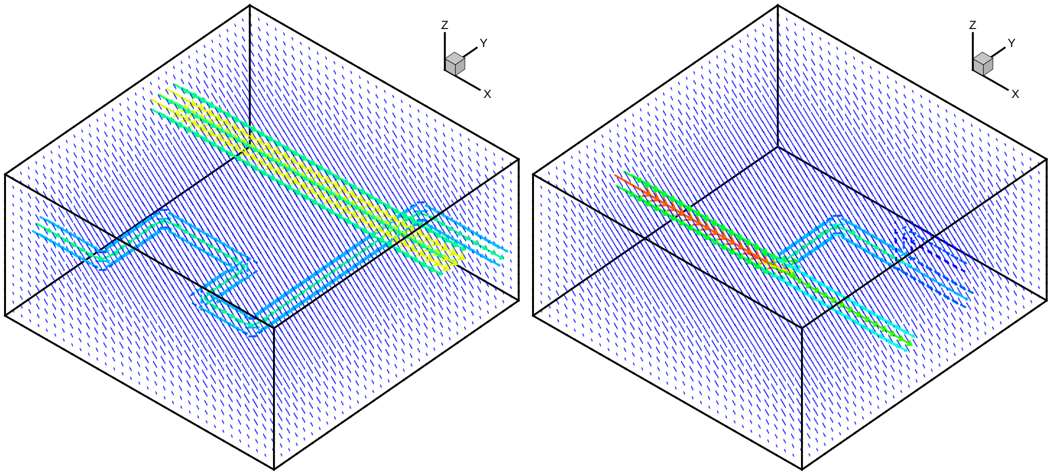

Figure 5.14: *On the left, there are two independent flow paths. On the right, a channel branches out into three flow paths.*

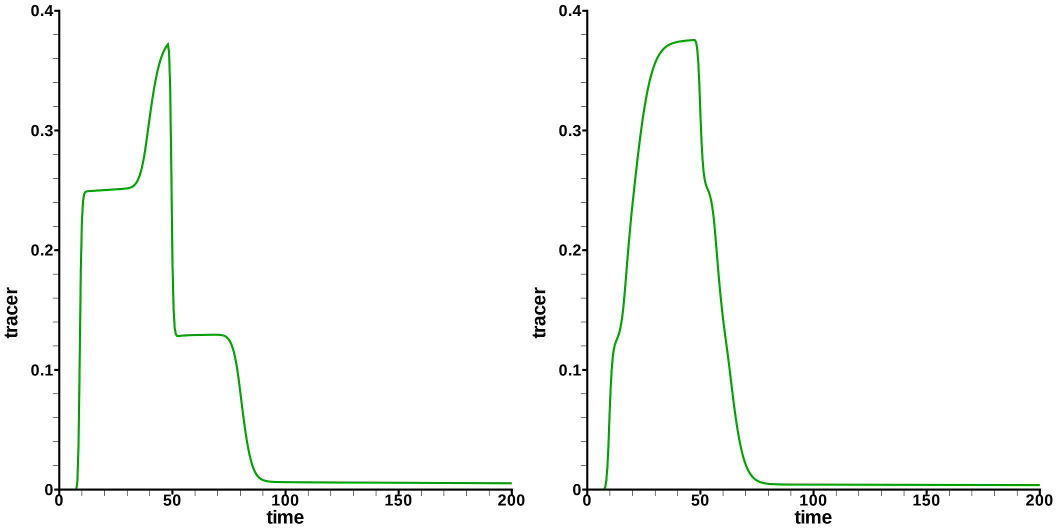

Figure 5.15: *Tracer mass histories corresponding to multiple paths (left) and multiple branches (right).*

5.2.4 Dead-end vugs

We now analyze the presence of dead-end vugs, which are also abundant in carbonates in general, and the Pipe creek sample in particular. Figure 5.16 shows a dead-end vug connected to the main flow path near the kink in the main channel. If one looks closely, flow in the dead-end vug can be seen, but the fluid is relatively stagnant there. It seems that the tracer accumulated here to some extent, and contributed a small pulse later in time when the main path ceased to carry significant mass of tracer. This very small "plateau" in the mass history can be seen in Figure 5.17. Notice that this effect is relatively small compared to the effect observed in the previous cases. We obtain similar results for many other geometries of dead-end vugs. Therefore, we believe that dead-end vugs connected to main flow paths play only a secondary role in the formation of the single plateau observed in Figure 5.4.

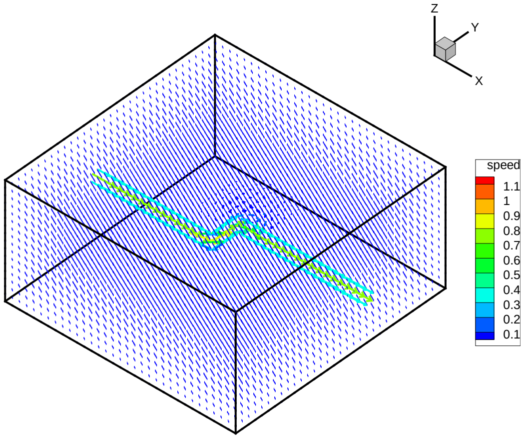

Figure 5.16: *Dead-end vug connected to the main flow path. Notice that the flow is relatively stagnant in the dead-end vug.*

5.2.5 Disconnected vugs

We also analyzed the case of disconnected vugs. These are vugs which are totally surrounded by porous matrix and have no direct connection to main flow paths. This is illustrated in Figure 5.18. The presence of the vug is not apparent from the flow field, since the flow in the disconnected vug is

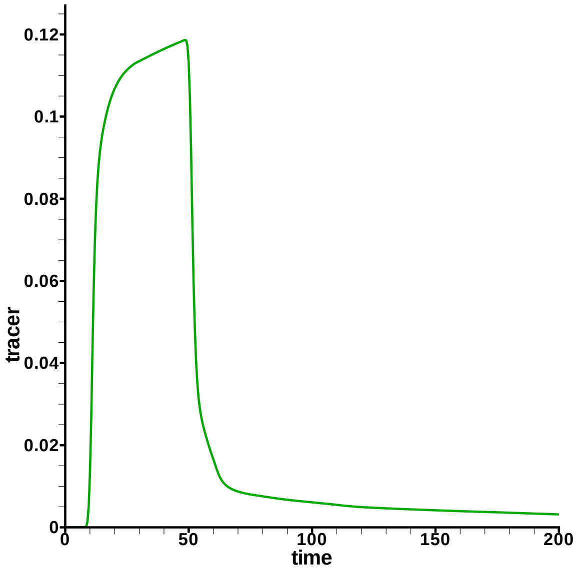

Figure 5.17: *Tracer mass history obtained for the flow of Figure 5.16. Dead-end vugs seem to have a minor effect on the formation of the single plateau.*

of the same magnitude as that in the Darcy region. We observed that these disconnected vugs made no contribution to the formation of plateaus in the effluent tracer mass history, at least for the time scales under consideration (compare with Figure 5.6). Together with the porous matrix, disconnected vugs presumably contribute to the long tail of the mass history. The stagnant fluid in this areas gradually seeps into the main paths.

5.2.6 Combinations of different configurations

So far we have analyzed simple cases separately, but all of these patterns are present in the rock. We next construct an example where the sample we simulate contains combinations of the vug patterns presented above. The flow shown in Figure 5.19 and the mass history of Figure 5.20 correspond to a sample containing multiple paths, multiple branches, bypass features and

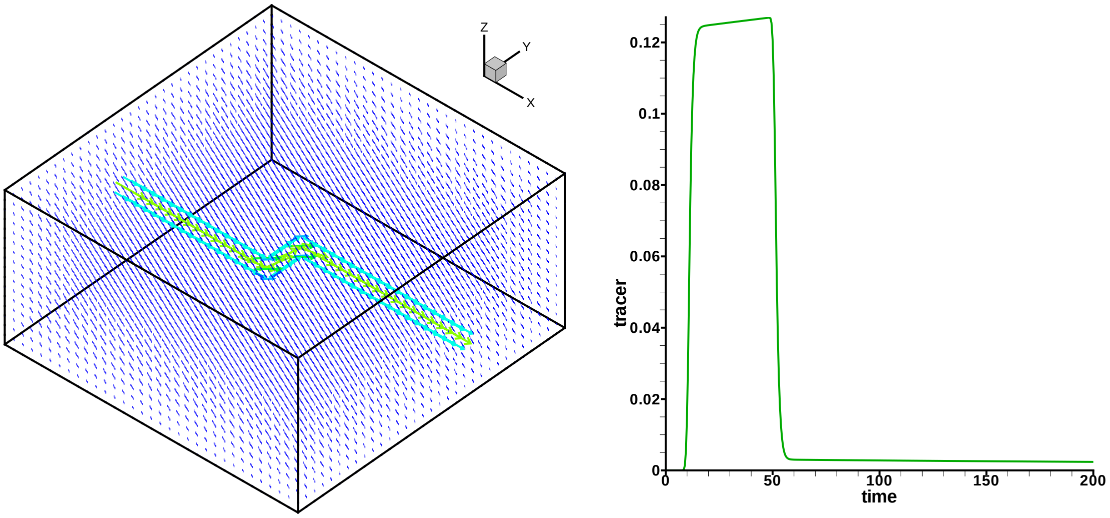

Figure 5.18: *Left: A vug is completely separated from the main flow path. The flow in a disconnected vug is of the same order of magnitude as that in the porous matrix. Right: The effluent mass history.*

dead-end vugs. Although not very evident, there is more that one component in the ascending part of the mass history curve. We also observe a plateau after the descending part of the curve which looks similar to the one of the experimental plot (Figure 5.4).

As we mentioned above, our previous simulations suggested that dead-end vugs play a secondary role in the formation of the single plateau. We can add more computational evidence to that conclusion by removing the dead-end vugs from the sample previously simulated and observing the change in the tracer mass history. The result is shown in Figure 5.21. Notice that the mass history has not changed after removing the dead-end vugs. Alternatively, if we remove from the original sample the bypass, multiple branches and multiple paths and keep a single path with several dead-end vugs, we obtain the tracer mass history shown in Figure 5.22. We can hardly see plateaus in this case.

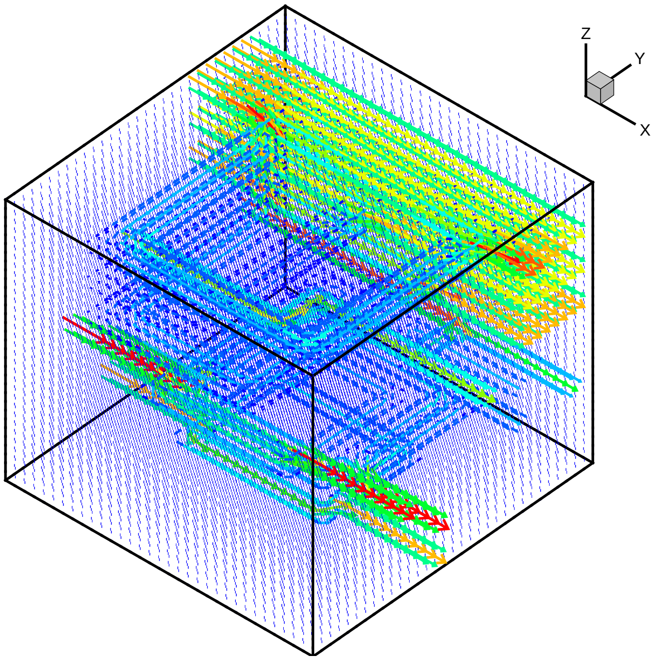

Figure 5.19: *Computed flow for a sample containing bypass branches, multiple branches and dead-end vugs.*

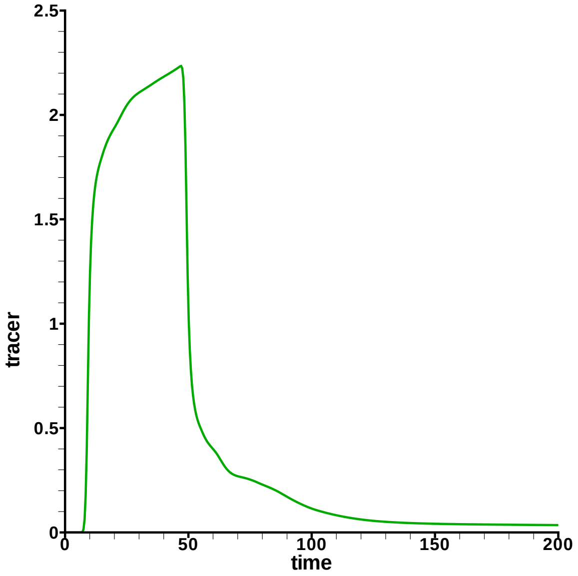

Figure 5.20: *Effluent tracer mass history for the flow of Figure 5.19.*

Therefore, we confirm that the main contribution to the formation of plateaus comes from bypass features, branching paths and multiple, separate paths, while dead-end vugs have only a small effect.

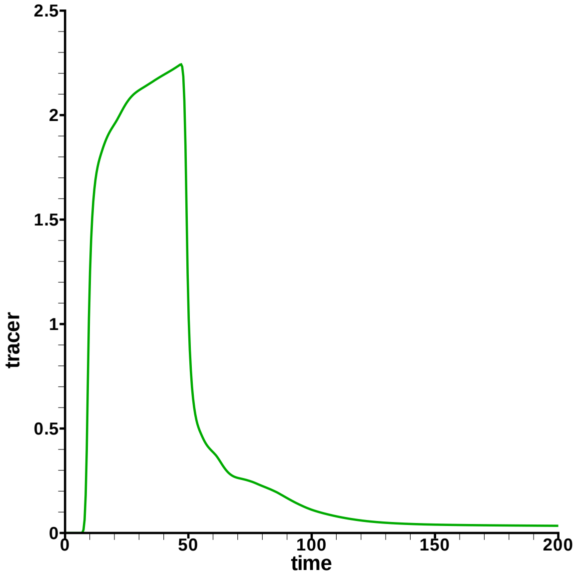

Figure 5.21: *Effluent tracer mass history for the same sample as in Figure 5.20 after removing dead-end vugs. Both mass histories are almost identical.*

We also simulated a sample containing only bypass branches of different types. The flow and the tracer mass history are shown in Figures 5.23 and 5.24 respectively. Because of the similarity with the experimental plot, we believe that bypass features have a major effect in the formation of plateaus.

To summarize, the tracer tests led us to the following conclusions:

1. On the time scales analyzed, all phenomena can be explained by the connected vug network while separate vugs have no real effect;
2. Plateaus can be formed by bypass features, branching paths, and multiple, separate paths;
3. Dead-end branches have only a small effect on the formation of plateaus.

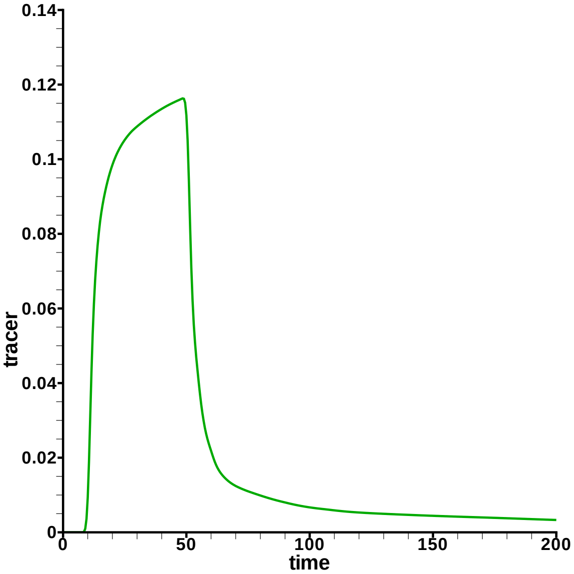

Figure 5.22: *Tracer mass history obtained for a sample with one flow path and multiple dead-end vugs.*

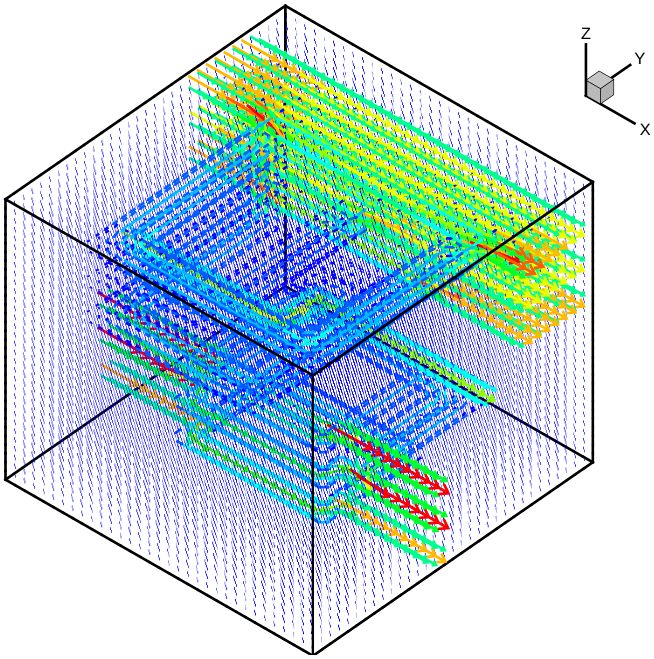

Figure 5.23: *Flow corresponding to a sample with several bypass features, but no dead-end vugs or multiple branches.*

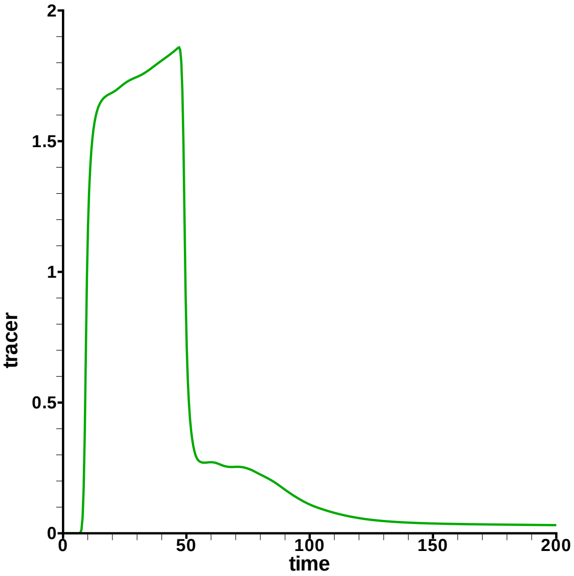

Figure 5.24: *Tracer mass history obtained for the sample of Figure 5.23, which contains several bypass features, but no dead-end vugs or multiple branches.*

That is, the initial multiple plateaus are directly associated with the single plateau that appears after the abrupt drop-off in the mass history curve, and not to dead-end vugs or some more complex mechanism.

Chapter 6

Numerical Studies of Flow Properties of Vuggy Media

In this chapter, we study the influence of the vug geometry on the flow properties of the medium. Our computational analysis is based on a macro-model developed in [6]. The Darcy-Stokes system described by (2.1)–(2.10) can be considered as a micro-model, since it takes into account all the details about the geometry of the medium and the interaction between the porous rock and the vugs, and the equations are either based on first principles or strongly supported by experiments. However, this model is computationally expensive. The macro-model derived in [6] is obtained from micro-model (2.1)–(2.10) appropriately scaled, using homogenization theory under certain mathematical assumptions.

This macroscopic model is given by a Darcy equation with an effective permeability tensor that depends on the vug geometry. Although some of the mathematical assumptions used in this derivation, such as the periodicity of the medium, are not physically accurate, the model is useful for investigating the influence of the vug geometry on the flow properties of the medium. This was shown in [4] and [5] in two dimensional space. Here, we do a similar investigation in three dimensions and arrive to similar conclusions. We observe that vug connectivity is the main factor influencing the macroscopic flow properties of a vuggy medium. We explore four types of configurations, but before we present our computational results, a brief description of the macro-model derived in [6] is given.

6.1 Homogenization of the Darcy-Stokes system and a macro-model

In order to apply the mathematical theory of homogenization, it is assumed in [6] that for each $\epsilon > 0$, the vug and pore structure of domain Ω is periodic with period ϵY. Here Y is a unit reference cell, which consists of a porous rock subdomain, Y_d, and a vug subdomain, Y_s, which are both periodic and share a common boundary, Γ. Then, the domain Ω consists of a porous rock subdomain Ω_d^ϵ and a vug subdomain Ω_s^ϵ. Since the vugs are constricted as $\epsilon \to 0$, the viscosity μ is scaled by ϵ^2 in order to maintain flow rates. This forces a similar scaling for the permeability K. A similar system of equations to (2.1)–(2.10) with the corresponding scaling, posed in Ω_d^ϵ and Ω_s^ϵ, is obtained for each ϵ.

It is proved in [6] that as $\epsilon \to 0$, the velocity $\bar{\mathbf{u}}^\epsilon$ and the pressure p^ϵ converge to the solution ($\bar{\mathbf{u}}$, p) of the Darcy equation

$$\mu \tilde{K}^{-1}\bar{\mathbf{u}} + \nabla p = f \quad \text{in } \Omega, \tag{6.1}$$

$$\nabla \cdot \bar{\mathbf{u}} = g \quad \text{in } \Omega. \tag{6.2}$$

Equations (6.1)–(6.2) represent the macro-model. The effective permeability tensor $\tilde{K}$ is given by

$$\tilde{K}_{i,j} = \frac{1}{|Y|}\left\{ \int_{Y_d} (w_j^d)_i \, dy + \int_{Y_s} (w_j^s)_i \, dy \right\}, \quad i,j = 1,2,3, \tag{6.3}$$

where ω_j^d and ω_j^s are the solutions (together with ϕ_j^d and ϕ_j^s) of the cell problem

$$-2\nabla \cdot D\omega_j^s + \nabla\phi_j^s = e_j \qquad \text{in } Y_s, \tag{6.4}$$

$$\nabla \cdot \omega_j^s = 0 \qquad \text{in } Y_s, \tag{6.5}$$

$$K^{-1}\omega_j^d + \nabla\phi_j^d = e_j \qquad \text{in } Y_d, \tag{6.6}$$

$$\nabla \cdot \omega_j^d = 0 \qquad \text{in } Y_d, \tag{6.7}$$

$$\omega_j^s \cdot \nu = \omega_j^d \cdot \nu \qquad \text{on } \Gamma, \tag{6.8}$$

$$2\nu \cdot D\omega_j^s \cdot \tau_\ell = -\frac{\alpha}{\sqrt{K}}\omega_j^s \cdot \tau_\ell \quad \text{on } \Gamma, \tag{6.9}$$

$$2\nu \cdot D\omega_j^s \cdot \nu = \phi_j^s - \phi_j^d \qquad \text{on } \Gamma. \tag{6.10}$$

In the cell problem (6.4)–(6.10), e_j denotes the jth unit vector in $\mathbb{R}^3$, ν is the outer unit normal to Y^s on Γ, and τ_ℓ are unit tangents to Γ.

6.2 Vug geometry and effective permeability

In this section, we present several computational results that show the influence of the vug geometry on the effective permeability in three dimensional space. In each of the cases we analyze, we consider a reference cell Y with a certain vug configuration. Four cases are studied: layered vugs, meandering channels, constricted channels, and disconnected vugs. The cell Y is a cubic sample with dimensions 8 cm × 8 cm × 8 cm, the porous rock subdomain Y_d has permeability $K = 10$ md, and the Beavers-Joseph coefficient $\alpha = 1$.

To compute the effective permeability, instead of solving cell problem (6.4)–(6.10), we use the fact, ensured by the homogenization result, that our system behaves at a macroscopic level as a Darcy system. Hence, we can estimate the diagonal elements of the effective permeability tensor in a simpler way. To fix our ideas, suppose we want to estimate the effective permeability in the x-direction, $\bar{K}_{1,1}$, the formula being analogous for the other directions. Using our three dimensional solver, we first compute the flow $\mathbf{u} = (u_1, u_2, u_3)$ in the reference cell that results from applying boundary conditions representing a constant pressure gradient $\nabla p = (\partial_1 p, 0, 0)$ in the x-direction, and imposing zero normal flow through the reference cell boundary faces which are parallel to the x-direction. We then compute the average flow in the x-direction through the inflow or outflow face f_x, which is

$$u_{1,av} = \frac{1}{m(f_x)} \int_{f_x} u_1(x, y, z)\, dy\, dz, \tag{6.11}$$

where $m(A)$ is the Lebesgue measure of a subset of $\mathbb{R}^2$.

By mass conservation, the zero normal flow boundary condition implies that the integral in (6.11) is independent of the face f_x that we choose; however, we always choose the face through which the fluid flows out of the cell. We note also that $u_{1,av}$ equals the average of u_1 over the whole cell. Finally, we define $\bar{K}_{1,1}$ from Darcy's law

$$\bar{K}_{1,1} = -\mu u_{1,av} / \partial_1 p \approx \tilde{K}_{1,1}. \tag{6.12}$$

We remark that we have not proved that this value for the effective permeability is equal to that given by (6.3). However, from a physical point of view, such an estimate of $\tilde{K}$ should give enough information about the influence of the vug geometry on the large-scale flow properties of the medium. The results of our simulations, which are now presented, confirm this intuitive idea.

6.2.1 Layered vugs

Figure 6.1 shows a two dimensional representation of the structure of the periodic cell and the periodic medium that results from it. The cell Y contains a horizontal channel. The channel's cross section is a square of side δ. We first examine the effective permeability for different vug apertures. The results are shown in Table 6.1. The index $j = 1$ in $\bar{K}_{j,j}$ corresponds to the horizontal or x-direction, $j = 2$ and $j = 3$ correspond to the y- and z-directions, respectively. We observe that connected Stokes flow paths produce a great increase in the effective permeability. Even a channel with an aperture $(2.5 \text{ mm})^2$ gives rise to an effective permeability 5 orders of magnitude larger than the porous rock permeability. The values of $\bar{K}_{2,2}$ and $\bar{K}_{3,3}$ for the effective permeabilities in the y- and z-directions, show that a disconnected Stokes flow path has a minor effect on the effective permeability, since the flow is limited by the porous matrix.

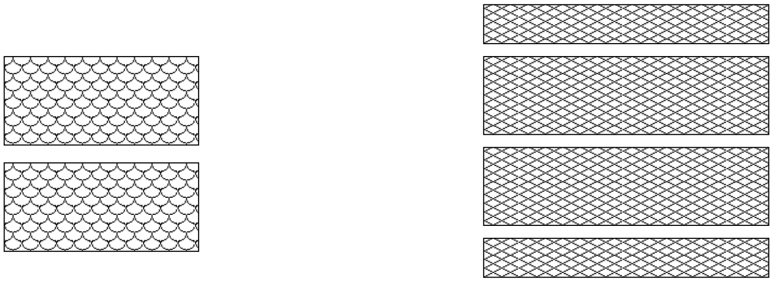

Figure 6.1: *Layered medium. The reference cell is on the left and the periodic medium is on the right.*

We also changed the porous rock permeability K, while keeping the same vug aperture $\delta = 1$ cm. As shown in Table 6.2, the effect of the presence of the channel on $\bar{K}_{1,1}$ is much more important than that of a high rock perme-

δ (cm)	$\bar{K}_{1,1}$ (md)	$\bar{K}_{2,2}$ (md)	$\bar{K}_{3,3}$ (md)
1	8.6498e+8	16.879	16.879
0.5	5.0856e+7	11.271	11.271
0.25	3.4560e+6	10.246	10.246

Table 6.1: *Computed effective permeabilities for a layered medium.*

K (md)	$\bar{K}_{1,1}$ (md)	$\bar{K}_{2,2}$ (md)	$\bar{K}_{3,3}$ (md)
1	8.64979e+8	1.6896	1.6896
10	8.64982e+8	16.879	16.879
100	8.64997e+8	168.50	168.50
1000	8.65104e+8	1685.1	1685.1

Table 6.2: *Effect of changing the rock matrix permeability on the effective permeability of a layered medium.*

ability. On the other hand, since the flow in the y- and z-directions is basically determined by the porous matrix, the value of the matrix permeability K has a stronger effect on the effective permeabilities $\bar{K}_{2,2}$ and $\bar{K}_{3,3}$.

6.2.2 Constricted channels

The aperture of a vug channel does not remain constant throughout its trajectory. Therefore, we analyze the effect of constricted vugs on the effective permeability. Figure 6.2 shows a cell with a central vug that is constricted in the middle. The aperture of the vug is 1 cm × 1 cm. The constricted part is 2 cm long and has cross section 2.5 mm × 2.5 mm. We obtained $\bar{K}_{1,1}$ = 7.85507e+6 md, $\bar{K}_{2,2}$ = 15.1971 md, and $\bar{K}_{3,3}$ = 15.1971 md. If we compare this values with the effective permeabilities for the unconstricted vug configuration ($\bar{K}_{1,1}$ = 8.64982e+8 md, $\bar{K}_{2,2} = \bar{K}_{3,3}$ = 16.879 md), we conclude that even very localized constrictions have a major effect on the macroscopic properties of the flow. Moreover, the value of $\bar{K}_{1,1}$ obtained for a 2 cm long constriction is of the same order of magnitude as that obtained for a layered medium with channels 2.5 mm × 2.5 mm ($\bar{K}_{1,1} = 3.4560\text{e}{+}6$ md, $\bar{K}_{2,2} = \bar{K}_{3,3} = 10.246$ md). This confirms the important effect of constrictions on effective permeability.

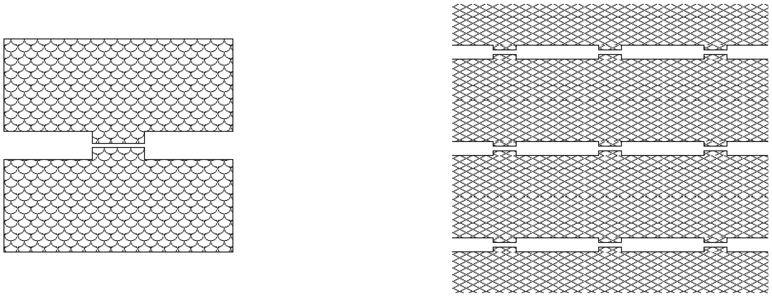

Figure 6.2: *Constricted vugs.*

6.2.3 Meandering vugs

Since natural vug channels tend to change their direction, we consider a meandering vug configuration. We study two cases. The first case is analogous to the two dimensional case since the meandering vug channel stays on the same plane throughout its trajectory. In the second case, the channel does not remain on the same plane.

The first case is illustrated in Figure 6.3. If a pressure gradient is applied in the x-direction, the flow through the channel will be in the x- and z-directions. The channel has cross section 1 cm × 1 cm. The effective permeabilities are $\bar{K}_{1,1} = 2.46928\text{e}{+}7$ md, $\bar{K}_{2,2} = 16.967$ md, and $\bar{K}_{3,3} = 19.3631$ md. We notice that $\bar{K}_{1,1}$ is smaller and $\bar{K}_{3,3}$ is larger than those values obtained for the layered case ($\bar{K}_{1,1} = 8.64982\text{e}{+}8$ md, $\bar{K}_{2,2} = \bar{K}_{3,3} = 16.879$ md), as should be expected.

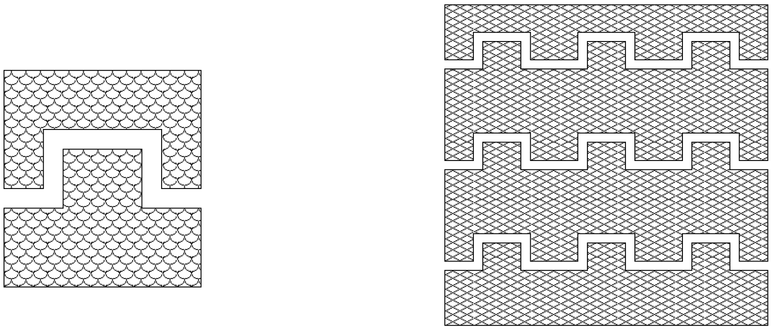

Figure 6.3: *Meandering vugs.*

The second meandering configuration is shown in Figure 6.4. If a pressure gradient is applied in the x-direction, the flow through the channel will be in the three spatial directions. We obtain $\bar{K}_{1,1} = 1.64619\text{e}{+}6$ md, $\bar{K}_{2,2} = 18.465$ md, and $\bar{K}_{3,3} = 18.589$ md. The value for $\bar{K}_{1,1}$ is lower than that for the previous meandering configuration and of the same order of magnitude as that obtained for the constricted vug ($\bar{K}_{1,1} = 7.85507\text{e}{+}6$ md, $\bar{K}_{2,2} = \bar{K}_{3,3} = 15.1971$ md). Note also the increase in the effective permeabilities in the y- and z-directions compared to the layered medium. These results show that in three dimensions, the effect of meandering channels is more complex than in the two dimensional case. Also, three dimensional meandering vugs and constricted vugs may have similar effects on the flow properties of vuggy media.

6.2.4 Disconnected vugs

Flow experiments suggest that the degree of vug connectivity varies throughout a vuggy porous medium and that it has a major effect on the flow properties of the rock [32]. Lastly we consider a configuration where the flow through a channel is completely interrupted by a small plug of porous rock. This is

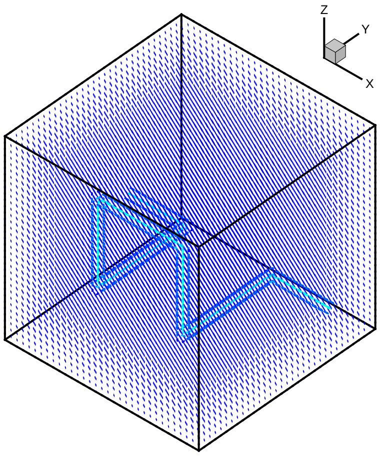

Figure 6.4: *Meandering vug in three dimensional space. Only the reference cell is shown.*

plug length (cm)	$\bar{K}_{1,1}$ (md)	$\bar{K}_{2,2}$ (md)	$\bar{K}_{3,3}$ (md)
0.25	88.69	17.27	17.28
0.5	50.63	17.01	17.02
1	38.54	16.92	16.92

Table 6.3: *Effect of disconnected vug by plug of varying size on effective permeability.*

depicted in Figure 6.5. The vug aperture is 1 cm × 1 cm and the plug length varies from 2.5 mm to 1 cm. The effective permeabilities are shown in Table 6.3. We notice that even if the length of the plug is 2.5 mm, the effective permeability is quite similar to that of the porous rock. We had seen that a vug with a very small constriction produces an effective permeability of about 1e+6 md, indicating that connected and disconnected vugs give rise to very different macroscopic flow properties. We conclude that the degree of connectivity of the vugs is the most important factor influencing the macroscopic flow properties of the medium.

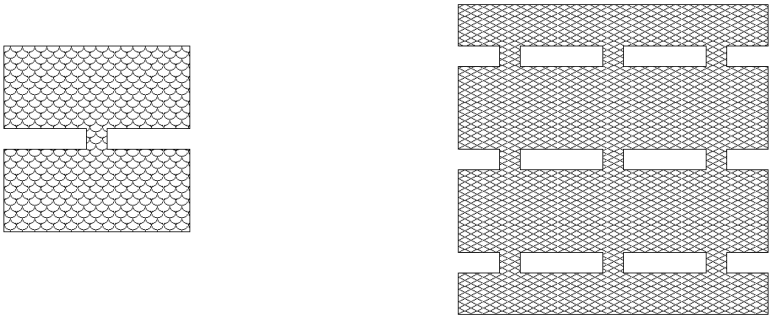

Figure 6.5: *Disconnected vugs.*

6.3 Summary

Although homogenization theory is based on a number of mathematical assumptions that are not physically justified, it turns out to be a useful tool to study the influence of vug geometry on the large-scale flow properties of a vuggy porous medium. At a macroscopic level, the flow can be described by Darcy's law via an effective permeability which strongly depends on the vug geometry. Our three dimensional numerical studies confirm that the presence of vugs, their orientation and shape, and most importantly, their interconnectivity, determine the effective permeability and, therefore, the macroscopic flow properties of the medium.

Chapter 7

Summary, Conclusions, and Future Work

Flow in a three dimensional vuggy porous medium is modeled by a system of partial differential equations where flow in the vugs and porous matrix is described by Stokes equation and Darcy's law, respectively, coupled by the Beavers-Joseph-Saffman boundary condition at the Darcy-Stokes interface. The differential system is discretized in three dimensions using modified Stokes elements. Degrees of freedom are removed from corners of elements near the Darcy-Stokes interface. Since we are interested in the three dimensional case where the size of such systems grows fast under grid refinement, we prefer to use the lowest order finite element method, where corners are also removed in the Darcy subdomain.

Since the Darcy and Stokes subdomains are intertwined, the resulting matrix is highly oscillating and ill-conditioned, and the solution of the corresponding linear system is also very irregular, with jumps of several orders of magnitude between neighboring points. The ill-conditioned nature of the matrix determines a very slow convergence rate for most iterative procedures used to solve the system. We solved this problem by using a multigrid method. Because the differential equation we are trying to solve might change totally from one grid element to the next, and because of the irregularity of the solution (its tangential component is discontinuous on the Darcy-Stokes interface), we needed to find a new way to define the intergrid prolongation operator. This was accomplished by considering coarse-grid quantities that approximately describe fluxes, doing a model-based analysis of the orders of magnitude of the solution in different subdomains, and imposing mass conservation principles. Our prolongation is a block diagonal operator that does not mix velocities and pressures. Our coarse-grid equations form saddle point systems. We proved that they are well posed at all grid levels.

Using a rather intricate Darcy-Stokes system, we showed that if no disconnected vug is present, the measured convergence factor of our multigrid method is apparently independent of the size of the system. If disconnected vugs are present, then our method does not perform as well and the measured convergence factor depends in general on the size of the system. We do not have an explanation for this phenomenon, but we plan to address it in future studies. Despite the decreased convergence factor in the case of domains with disconnected vugs, our method was still effective for solving this type of system in our simulations.

A new smoother of Uzawa type was developed to smooth the saddle point system. It is better suited for our ill-conditioned problem, because it is less sensitive to having good preconditioners.

One of the main advantages of our multigrid method is that it can be used in a parallel code. This would open the possibility of doing simulations of large systems representing realistic vuggy porous media, with vug patterns obtained from rock samples by X-ray computed tomography scans. This is planned for future work.

Once we had developed our three dimensional flow solver, we could complete a computational study investigating the transport properties of vuggy media. We analyzed several vug configurations. For each of them, we run a simulation in which a pulse of tracer was injected into the sample and the effluent tracer mass history was observed. We then compared the shape of our mass history with experimental results, focusing our attention on the presence of plateaus. We concluded that plateaus during the initial rise of effluent tracer mass and right after the rapid descent are produced by the connected vug network, while disconnected vugs play no role in their formation. Vug configurations with bypass features, multiple branches and multiple paths have a major effect on the formation of plateaus, while dead-end vugs are shown to have just a minor effect.

Finally, we investigated the influence of vug geometry on the flow properties of three dimensional vuggy media. We used a macro-model obtained from homogenization theory in which flow in a vuggy medium is described by Darcy's law with an effective permeability that depends on the vug geometry. Using our solver, we estimated the effective permeability for different vug configurations, by computing the average flow in a reference cell under a pressure gradient and applying Darcy's law. Our results were consistent with those obtained by other authors in the two dimensional case. The presence of connected channels increases the effective permeability by several orders of magnitude. This is true even for very narrow channels, though the wider the channel, the larger the effective permeability. Channel constrictions are also important, since the effect of vugs with very small constrictions is nearly equivalent to that of channels which are narrow along the whole trajectory. The effect of meandering vugs is more complex in three dimensions and sometimes comparable to that of constricted channels. The most important factor is the degree of connectivity of the vugs. A very small plug of porous matrix disconnecting a vug has almost the same effect as having no vug at all.

As we mentioned above, the next step in our future research program will be to develop a parallel code based on our multigrid method, so that we can perform more realistic simulations of larger Darcy-Stokes systems. We would like to understand the behavior of our method when disconnected vugs are present, and to make improvements to increase the rate of convergence in such cases. We are also interested in studying transport phenomena over long time scales.

Bibliography

[1] E. Anderson, Z. Bai, C. Bischof, S. Blackford, J. Demmel, J. Dongarra, J. Du Croz, A. Greenbaum, S. Hammarling, A. McKenney, D. Sorensen. *LAPACK Users' Guide, third edition.* Society for Industrial and Applied Mathematics, 1999.

[2] R.E. Alcouffe, A. Brandt, J.E. Dendy, J.W. Painter. *The multi-grid method for the diffusion equation with strongly discontinuous coefficients.* SIAM J. Sci. Comput., **2**, 430–454, 1981.

[3] T. Arbogast. *User's Guide to Parssim1: The Parallel Subsurface Simulator, Single Phase.* The Center for Subsurface Modeling, Texas Institute for Computational and Applied Mathematics, The University of Texas at Austin, Austin, Texas, TICAM Report 98–13, May, 1998.

[4] T. Arbogast, D.S. Brunson. *A computational method for approximating a Darcy-Stokes system governing a vuggy porous medium.* Computational Geosciences, 2007, to appear.

[5] T. Arbogast, D.S. Brunson, S.L. Bryant, J.W. Jennings. *A preliminary computational investigation of a macro-model for vuggy porous media.* In Computational Methods in Water Resources XV, C.T. Miller et al., eds., Elsevier, New York, 2004.

[6] T. Arbogast, H.L. Lehr. *Homogenization of a Darcy-Stokes system modeling vuggy porous media*, Computational Geosciences, **10**, 291–302, 2006.

[7] T. Arbogast, M.F. Wheeler. *A family of rectangular mixed elements with a continuous flux for second order elliptic problems.* SIAM J. Numer. Anal., **42**, 1914–1931, 2005.

[8] J. Bear. *Dynamics of Fluids in Porous Media.* Dover, New York, 1972.

[9] G. S. Beavers and D. D. Joseph. *Boundary conditions at a naturally permeable wall.* J. Fluid Mech., **30**, 197–207, 1967.

[10] J.H. Bramble, J.E. Pasciak. *A preconditioning technique for indefinite systems resulting from mixed approximations of elliptic problems.* Math. Comp., **50**, 1–17, 1988.

[11] J.H. Bramble, J.E. Pasciak, A.T. Vassilev. *Analysis of the inexact Uzawa algorithm for saddle point problems.* SIAM J. Numer. Anal., **34**, 1072–1092, 1997.

[12] A. Brandt. *Multi-level adaptive solutions to boundary-value problems.* Math. Comp., **31**, 333–390, 1977.

[13] F. Brezzi. *On the existence, uniqueness and approximation of saddle-point problems arising from Lagrangian multipliers.* RAIRO, **8**, 129–151, 1974.

[14] F. Brezzi, M. Fortin. *Mixed and hybrid finite element methods.* Springer-Verlag, New York, 1991.

[15] D. S. Brunson. *Simulating Fluid Flow in vuggy porous media*, Dissertation, Univ. of Texas at Austin, 2005.

[16] M. Fortin. *Old and new finite elements for incompressible flows.* Int. J. Numer. Meth. Fluids, **1**, 347–364, 1982.

[17] D. K. Gartling, C. E. Hickox, R. C. Givler. *Simulation of coupled viscous and porous flow problems.* Comp. Fluid Dyn., **7**, 23–48, 1996.

[18] W. Hackbusch, U. Trottenberg (eds). Multigrid Methods II. Lecture Notes

in Mathematics 1228, Springer, Berlin, 1986.

[19] I. P. Jones. *Low Reynolds number flow past a porous spherical shell*, Proc. Camb. Phil. Soc., **73**, 231–238, 1973.

[20] W. J. Layton, F. Schieweck, I. Yotov. *Coupling fluid flow with porous media flow.* SIAM. J. Numer. Anal., **40**, 2195–2218, 2003.

[21] D. W. Peaceman. *Fundamentals of numerical reservoir simulation.* Elsevier, Amsterdam, 1977.

[22] T. J. Petta. *Diagenesis and geochemistry of a Glenn Rose patch reef complex, Bandera County, Texas.* In Cretaceous carbonates of Texas and Mexico, Applications to subsurface exploration, D. G. Bebout and R. G. Loucks, eds., pp. 138–167, 1977.

[23] B. F. Perkins. *Paleoecology of a rudist reef complex in the Comanche Cretaceous Glen Rose Limestone of Central Texas.* In Aspects of Trinity Division geology, B. F. Perkins, ed., vol. 8 of Geoscience and Man, Louisiana State University, pp. 131–173, 1974.

[24] R. A. Raviart, J. M. Thomas. *A mixed finite element method for* 2*nd order elliptic problems.* In Mathematical Aspects of Finite Element Methods, Lecture Notes in Math. 606, I. Galligani and E. Magenes, eds., Springer-Verlag, New York, pp. 292–315, 1977.

[25] J.W. Ruge, K. Stüben. Algebraic multigrid (AMG). *Multigrid methods, Frontiers in Applied Mathematics*, S.F. McCormick, ed., SIAM, Philadelphia, pp. 73–130, 1987.

[26] P.G. Saffman. *On the boundary condition at the interface of a porous medium*, Studies in Applied Mathematics, **1**, 93–101, 1971.

[27] A. G. Salinger, R. Aris, J. J. Derby. *Finite element formulations for large*

scale, coupled flows in adjacent porous and open fluid domains. International Journal for Numerical Methods in Fluids, **18**, 1185–1209, 1994.

[28] K. Stüben. *A review of algebraic multigrid.* Numerical Analysis 2000, vol VII, Partial Differential Equations. J. Comput. Appl. Math., **128**, no 1–2, 281–309, 2001.

[29] L. Tartar. *Incompressible fluid flow in a porous medium—convergence of the homogenization process.* In Non-homogeneous Media and Vibration Theory, E. Sanchez-Palencia, Lecture Notes in Physics 127, Springer-Verlag, Berlin, pp. 368–377, 1980.

[30] U. Trottenberg, C. Oosterlee, A. Schüller. *Multigrid.* Academic Press, 2001.

[31] S. Whitaker. *Flow in porous media I: A theoretical dedrivation of Darcy's law.* Transport in Porous Media, **1**, 3–25, 1986.

[32] L. Zhang. *Multiscale flow and transport in highly heterogeneous carbonates.* Dissertation, U. of Texas at Austin, 2005

Vita

Mario San Martin Gomez was born May 2, 1968 in Havana to parents Antonio and Maria. He received his Bachelors of Science degree in Mathematics from Havana University in 1997. He is currently pursuing his Ph.D. in Mathematics at the University of Texas at Austin.

Permanent address: 3500 Benny Ave
Montreal, Quebec
Canada H4B 2R8

This dissertation was typeset with LaTeX[‡] by the author.

[‡] LaTeX is a document preparation system developed by Leslie Lamport as a special version of Donald Knuth's TeX Program.